Reviews in Mineralogy & Geochemistry
Vol. 89 pp. 563-609, 2023

The Dust, Atmosphere, and Plasma at the Moon

William M. Farrell [*,1], Jasper S. Halekas[2], Mihaly Horányi[3], Rosemary M. Killen[1], Cesare Grava[4], Jamey R. Szalay[5], Mehdi Benna[1], Pamela E. Clark[6], Michael R. Collier[,1], Anthony Colaprete[7], Jan Deca[15], Richard C. Elphic[7], Shahab Fatemi[8], Yoshifumi Futaana[9], Mats Holmström[9], Dana M. Hurley[10], Georgiana Y. Kramer[11], Paul R. Mahaffy[1], Masaki N. Nishino[12], Sarah K. Noble[13], Yoshifumi Saito[12], Andrew R. Poppe[14], Kurt D. Retherford[4], Xu Wang[15], Shoichiro Yokota[16]**

**Retired, **Deceased*

[1]NASA Goddard Space Flight Center 8800, Greenbelt Road, Greenbelt, MD, 20771 USA

[2]Department of Physics and Astronomy, University of Iowa, Iowa City, IA, 52242 USA

[3]Department of Physics,University of Colorado, Boulder, CO 80309, USA

[4]Southwest Research Institute, 6220 Culebra Road, San Antonio, TX, 78238, USA

[5]Department of Astrophysical Sciences, Princeton University, Peyton Hall, 4 Ivy Lane, Princeton, NJ, 08544, USA

[6]Department of Physics, Earth Science and Space Science Engineering, Morehead State University, 123 Lappin Hall, Morehead, KY, 40351, USA

[7]NASA Ames Research Center, Space Science Division, Moffett Field, Mountain View, CA 94035, USA

[8]Department of Physics, Fysikhuset, plan 4, Linnaeus väg 24, FA419, Umeå Universitet, 901 87 Umeå, Sweden

[9]Swedish Institute of Space Physics, Bengt Hultqvists väg 1, 981 92 Kiruna, Sweden

[10]Johns Hopkins University Applied Physics Laboratory, 11100 Johns Hopkins Road, Laurel, MD, 20723, USA

[11]Planetary Science Institute, Tucson, AZ, 85719, USA

[12]Institute of Space and Astronautical Science (ISAS), Japan Aerospace Exploration Agency (JAXA), Yoshinodai 3-1-1, Chuo-ku, Sagamihara, Kanagawa, 252-5210, Japan

[13]Mary W. Jackson NASA Headquarters, 300 Hidden Figures Way SW., Washington, DC, 20546, USA

[14]Space Sciences Laboratory, University of California, Berkeley, CA, 94720, USA

[15]Laboratory for Atmospheric and Space Physics (LASP), University of Colorado, Boulder, CO 80309, USA

[16]Osaka University, Machikaneyama-cho, Toyonaka 560-0043, Japan

1529-6466/23/0089-0013$05.00 (print)
1943-2666/23/0089-0013$05.00 (online)
http://dx.doi.org/10.2138/rmg.2023.89.13

1. INTRODUCTION

The topics of lofted dust, ejected atomic and molecular species, and plasma interactions at the Moon have made revolutionary strides since the last 'New Views of the Moon' review in 2006 (Jolliff et al. 2006). Specifically, in the last 13 years, there have been over a half-dozen spacecraft that are dedicated, wholly or in part, to the study of this neutral, ionized, and particulate atmosphere at the Moon. A key finding is that all three of these phenomena are inter-connected, and suggest the term 'exosphere' can be extended to particulates and surface-emitted plasma like reflected protons and exo-ions (Saito et al. 2008; Halekas et al. 2012a). We thus now view the Moon as enshrouded in a dusty, low-density, partially ionized gas emitted from the surface via meteoritic drivers and incident space plasma.

Figure 1 illustrates this new view of the component-extended exosphere around the Moon. Specifically, energy in the space environment including solar radiation, solar wind, cosmic rays, and constant micrometeoritic rain, is directly incident on the surface, impacting at small (atomic to millimeter) scales. In response to this environmental energy input, there is the formation of a neutral collisionless shroud of gas surrounding the Moon with scale heights of 100's of kilometers, inter-mixed with small particulates that have similar scale heights. In addition, there is both a modification of the flowing solar wind to form the trailing wake region and an added exo-ion and surface-emitted plasma component that can flow counter to the solar wind.

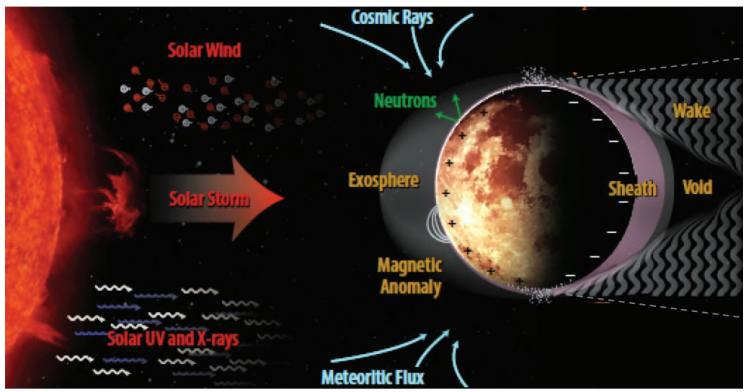

Figure 1. An illustration of the dust, neutral gas, and plasma enshrouding the Moon .

While some in the planetary community might consider the lunar surface to be stagnant or dead, investigators now realize that the surface is very dynamic at the microscopic level with modern external processes continually modifying the oxide-rich regolith. Consequently, the story of the dust, atmosphere, and plasma at the Moon is a story of the modern Moon. The long-term effects of these modern processes are found in the returned lunar samples. The manifestation of the continuous weathering in these samples, including the creation of nano-phase iron, the formation of crystal-disrupted grain rims, and the generation of impact-melted agglutinates thus allows a connection of the modern environmental processes discussed herein back in time to past activity. That connection is further discussed in Denevi et al. (2023, this volume).

As described in more detail in Gaddis et al. (2023, this volume) and below, the new dust, atmosphere and plasma observations are derived from recent international lunar missions including the Lunar Reconnaissance Orbiter (LRO) launched in 2009. Specifically, LRO flew the Lyman-Alpha Mapping Project (LAMP) in lunar orbit which searched for and discovered new neutral exospheric species. On the launch manifest with LRO was the Lunar Crater Observation and Sensing Satellite (LCROSS) that examined a human-created ejecta plume

released from the floor of Cabeaus crater. In 2007, Japan launched the Kaguya spacecraft that included a magnetometer and plasma instrument that discovered reflected plasma species, new plasma wake configurations, and large *E*-fields in magnetic anomalies. In 2008, India launched the Chandryaan-1 spacecraft that carried a Swedish-built particle instrument that mapped backscattered energetic neutral hydrogen and incident plasma at the lunar surface. In 2011, NASA's heliophysics division placed two existing magnetosphere-sensing spacecraft into a new orbit about the Moon to form the THEMIS-ARTEMIS lunar space plasma mission. These twin spacecraft made new findings on the Moon-created plasma structures, including the formation of the exo-ionosphere and extended wake in the solar wind. In 2013, NASA's planetary division launched the dedicated Lunar Dust and Atmosphere Environment Explorer (LADEE) mission which discovered new exospheric species, a new particulate shroud, and tracked volatile transport over the Moon.

In the last 13 years, NASA and its international partners have invested substantial funding and hardware assets—including the two THEMIS-ARTEMIS and the LADEE spacecraft—to the study of the neutral, dust, and plasma exosphere. Consequently, one chapter cannot cover in detail all of the stunning new findings. However, we do attempt herein to review the drivers that energize the surface and to describe the associated response in the form of the Moon-enshrouding layers, which are far more rich, complex and interconnected than imagined 13 years ago.

2. DRIVERS OF THE NEAR-LUNAR SPACE ENVIRONMENT

The near-lunar environment is affected by processes that eject atoms, molecules and dust into the exosphere from the surface. These processes include photon-stimulated desorption, thermal desorption, impact vaporization, reflection of solar wind protons, and bombardment by the solar wind (sputtering, surface charging, and surface chemistry). In this section we introduce the drivers of these processes: solar radiation, meteoritic influx and the solar wind.

2.1. Solar radiation

Solar radiation affects the lunar environment in a myriad of ways depending on the energy of the radiation and the chemical makeup of the species being irradiated. High energy radiation is characterized as ionizing radiation, and the species affected depend on their ionization potential (Elphic et al. 1991). Ultraviolet radiation is effective at desorbing relatively volatile elements such as sodium and potassium in a process called photon-stimulated desorption (PSD) (e.g., Yakshinskiy and Madey 1999, 2004).

Although the cross section for PSD increases with shorter wavelengths of light, the solar flux decreases rapidly in the effective regions (see Fig. 2) resulting in an effective wavelength range that typically requires a convolution of the two counter-varying parameters. The cross sections must therefore be integrated over the solar spectrum to obtain the accurate total ejection flux for species like Na and K.

The visible radiation impacting the Moon's surface mainly affects the thermal environment and space weathering of the surface (Domingue et al. 2014). There are many sources of measurements of the solar flux (Brault 1972; Neckel and Labs 1981; Simon 1981; Kurucz et al. 1984; Thuillier et al. 1998). Solar spectral irradiance in the UV from 30–2700 nm obtained from multiple spacecraft missions can be found at the Laboratory for Atmospheric and Solar Physics website: http://lasp.colorado.edu/lisird/. High resolution solar spectra can also be found (and plotted) from the Observatoire de Paris website: BASS2000.obspm.fr, which contains data from NIST (National Institute of Standards and Technology) and VAMDC (Virtual Atomic and Molecular Data Centre).

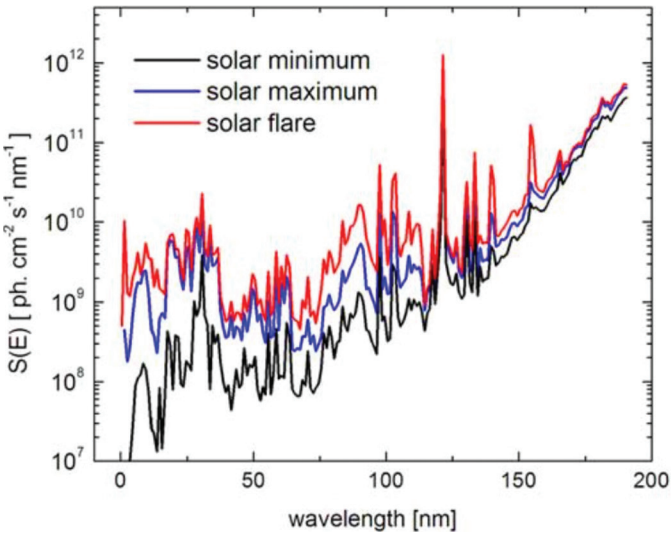

Figure 2. Variability in the FUV spectrum that influences PSD (from Sternovsky et al. 2008 and references therein).

2.2. Meteoroid environment

Another important driver of the near-lunar space environment is the continual bombardment of high-velocity meteoroids. At the Earth, meteoroids mainly ablate to form visible trains commonly known as 'shooting stars'. However, without a thick atmosphere, the Moon's surface is completely exposed to the entirety of the incident meteoroid flux. Each impact can produce orders of magnitude more solid ejecta mass than the primary impactor, making the ejecta response of the surface tightly connected to its local meteoroid environment. These ejecta clouds carry information about the composition of the lunar surface and the instantaneous state of meteoroid bombardment to that body, given the short timescales of ejecta plumes on the order of 10's of minutes. Impact processes redistribute the lunar surface material and can uncover and reblanket features on the lunar surface at varying timescales, a process called 'regolith gardening'. The impacts can also liberate appreciable quantities of neutral atoms and may play an important role in the dynamics of the lunar exosphere.

To understand the effects of meteoroid bombardment at the Moon, as will be discussed in subsequent sections, we briefly review the current state of knowledge of interplanetary dust particles (IDPs). The sources for these grains at 1 AU are predominantly Jupiter Family Comets (JFCs), however, Halley Type Comets (HTCs), Oort Cloud Comets (OCCs), and asteroids can also contribute an appreciable amount to the IDP environment. When grains are shed from their parent bodies, their orbital elements are initially similar to their parent's. In addition to the gravitational forces by the Sun and the planets, the dynamics of small dust particles are influenced by size-dependent forces, including solar wind and Poynting–Robertson drags, radiation pressure, and the Lorentz force.

The combination of these forces causes the ejected grains to decouple from their parent bodies and follow divergent trajectories over time. Under certain conditions, and more notably for larger grains, the particles can preferentially disperse along the trajectory of their parent body, and may fill its entire orbital loop to form a 'tube' of material. Once the orbit of a source body has been filled out, it becomes a potential meteor stream. If the Earth–Moon system intersects the ascending or descending node of this tube, it leads to a meteor shower that is named according to the constellation in the apparent direction or radiant of the shower.

Smaller grains that are more susceptible to non-gravitational perturbations tend to disperse, and follow orbits that rapidly diverge from their parent bodies. These grains comprise the 'sporadic background'. The sporadic background has its own structure and is organized by various radiant groupings: a) the helion/anti-helion (HE/AH); b) the apex/anti-apex (AP/AA); and c) the northern/southern toroidal (NT/ST) sources (Jones and Brown 1993; Janches et al. 2000; Campbell-Brown 2008). Each of the sporadic groupings has distinct sources, which leads to different characteristic radiants and impact velocities.

The study of IDPs has a long history involving observations of their emissions and absorptions in the optical to thermal infrared, in-situ measurements of dust through space based in-situ dust and plasma detectors, and Earth-based optical and radar observations of meteors. One of the early methods of quantifying interplanetary dust in the inner solar system was observation of the zodiacal emission from the dust in orbit about the Sun (e.g., Hahn et al. 2002). With the advent of space-based, dedicated dust detectors, satellites have been able to measure the dust in the inner solar system since the Helios 1 mission (Grün et al. 1980). The near-Earth environment was also monitored by the Long Duration Exposure Facility (LDEF) satellite, which allowed for estimates of the terrestrial mass accretion rate via analysis of impact craters on the spacecraft due to micrometeoroids (Love and Brownlee 1993).

The near-Earth environment was reviewed by McDonnell et al. (2001) including descriptions of meteoroid properties and dynamics, meteor streams, space debris and models. A time-averaged functional form for the interplanetary dust flux at 1 AU was derived using a synthesis of in-situ dust detection, zodiacal light observations, and lunar microcraters and is commensurate with the LDEF measurements after corrections are applied (Grün et al. 1985). More recently, ground-based networks have been able to further constrain the flux of particles to the Earth–Moon system. However, a large uncertainty still remains in the total mass flux, which has been found to be in the range of 5–270 tons per day (Plane 2012).

2.3. Solar wind

The solar wind consists primarily of sun-outflowing protons and electrons with nominal velocity near 400 km/second and nominal density at 1 AU near 5 particles/cm^3. The solar wind is coupled to the interplanetary magnetic field that has a nominal value at 1 AU of about 5 nT. However, the instantaneous values can vary greatly from the nominal. During the passing of a coronal mass ejection (CME), the speeds can double and the densities can increase by a factor of 5–10 (see Fig. 4 of Farrell et al. 2012). The typical solar wind plasma temperature is about 110,000 K (~10 eV). However, during a CME passage, this temperature can vary considerably being 2–3 times higher (20–30 eV) in the sheath region and 2–3 times cooler (< 5 eV) in the early CME period. Solar wind protons have an energy peak near 800 eV, but the time-averaged spectrum also has an energetic tail wherein the solar wind flux levels progressively decreased with increasing energy out to beyond 100 keV. This high energy tail can have an effect on space weathering and grain rim creation (Poppe et al. 2017).

The typical solar wind is comprised of 95% protons, 2–4% He, with the remainder made up of trace species of heavier ions (like O^{7+}). However, the solar wind composition has variability: during impulsive coronal mass ejections the relative concentration of heavy ions (He^{++}, O^{7+}, etc.) can increase to > 20%.

The solar wind is characterized by an 11-year solar cycle that is, however, not perfectly repeatable, especially in its maximum behavior from cycle to cycle. During solar maximum all quantities are more highly variable than during solar minimum. In addition, the composition and energy of the solar wind, although usually characterized by its mean, is also not constant. The slow solar wind is most often seen at low solar latitudes below 30^o but its range expands during solar maximum. There is a significant difference in composition between the fast and slow solar wind (Table 1 in von Steiger et al. 2000), and a shift toward higher charge states in the slow wind compared with the fast wind (von Steiger et al. 2000).

Solar energetic particle events (SEPs) are characterized by enhancements in high first ionization potential (FIP) elements, and CMEs are often enhanced in high charge state ions, which are highly effective as sputtering agents. Both solar wind and SEP events show a fractionation pattern organized by FIP, with considerable scatter (von Steiger et al. 2000). When compared to photospheric abundances, the SEP abundances of elements with FIP > 10 eV are depleted relative to those with lower FIP values (i.e., K, Na, Al, Ca, Cr, Ti, Mn, Mg, Co, Cu, Fe). Curiously these low FIP elements have all been seen in the Moon's exosphere. SEP events are also characterized by abundance variations that depend on the charge to mass ratio. The CME driver plasma is highly enriched in heavy elements such as Fe and Ne relative to both solar wind and SEP material. The cool solar wind ($O^{7+}/O^{6+} < 0.1$) is associated with coronal holes; hot ejecta ($O^{7+}/O^{6+} > 1.0$) are associated with Interplanetary CMEs (ICMEs) (Zurbuchen et al. 2002). ICMEs are characterized by abrupt transitions to higher charge states.

3. THE MOON'S RESPONSE TO THE DRIVERS

3.1. Neutral exosphere

The Moon possesses the ideal surface-bounded exosphere. It is a body that does not possess a collisional atmosphere. All planetary bodies possess some outer region containing a tenuous, collisionless atmosphere, where collisions among particles are negligible. Such regions may be the uppermost extent of a collisional atmosphere such as at the Earth, and borrows the same name: exosphere. Unlike Earth's exosphere, however, the lower boundary, or the exobase, of a surface-bounded exosphere is not another atmospheric layer (below which collisions happen). Instead, on the Moon, the exobase is the solid surface itself. Since collisions between particles are negligible, the dynamics of the exosphere depend on the interaction of the source with the surface, i.e., from the processes with which atoms and molecules are released. These processes are related to external drivers, such as solar flux, micrometeoroids, solar wind and other energetic particles and photons (e.g., extragalactic gamma rays and Lyman-alpha photons from the interplanetary medium), and internal drivers, such as thermal desorption and outgassing from the interior.

Surface-bounded exospheres are present on every airless body of the Solar System, notably Mercury, Europa, Enceladus, Ceres, and comets. Because of its proximity to Earth, the Moon is recognized as the best setting to study the interaction between a surface-bounded tenuous gas region and the external space environment. A concern is that future human activity during exploration, resource prospecting, and mining may substantially alter the very nature of the fragile exosphere. Consequently, LADEE was launched to obtain an inventory of the lunar dusty exosphere before human presence and occupation alters the environment. In this section, we summarize recent findings that expand and update the previous seminal review by Stern (1999).

3.1.1. Composition from LACE, LAMP, and LADEE. Helium and argon were discovered by the surface-based Lunar Atmosphere Composition Explorer (LACE) mass spectrometer deployed during the Apollo 17 mission (Hoffman et al. 1973). Their respective spatial and temporal variation were found to be very different in both origin and adsorption behavior. Helium density was correlated with the time of day, exhibiting a number density (n) dependence on surface temperature (T) typical of non-condensable gases: $n \sim T^{-2.5}$ (Hodges and Johnson 1968). In contrast, argon density showed a progressive decline on the nightside from dusk to dawn as more atoms were temporarily cold-trapped on the lunar surface and in pore spaces. The argon exospheric density then peaks after dawn, when the combination of freshly desorbed atoms and atoms that are escaping the hot dayside surface is maximized. The origin of these two species was also found to be different. Helium density was correlated with the solar wind (Hodges and Hoffman 1974); the mechanism to generate the lunar helium is the neutralization of alpha particles from the solar wind at the lunar surface. Argon detected by LACE was primarily ^{40}Ar, which was considered an endogenic gas, resulting from the

radioactive decay of ^{40}K within the crust. Unlike helium, ^{40}Ar showed sudden increases in the density, and these have been correlated with moonquakes. Neon was also detected by LACE and believed to be of solar wind origin (Hodges et al. 1974).

More recently, the Japanese spacecraft Kaguya observed sodium (Kagitani et al. 2010) that had previously been discovered, together with potassium, by ground-based telescopes (Potter and Morgan 1988; Tyler et al. 1988) via emission from resonant scattering. The same technique was used by the UV spectrograph, LAMP, on board of the Lunar Reconnaissance Orbiter (LRO) to detect He (Stern et al. 2012) and H_2 (Stern et al. 2013). LAMP observations also placed more stringent upper limits on numerous other species (Cook et al. 2013). Finally, LADEE launched in 2013 for a 223-day mission and carried three instruments: the Neutral Mass Spectrometer (NMS), the Ultraviolet and Visible Spectrometer (UVS), and the Lunar Dust Experiment (LDEX) that provided unprecedented new measurements of the lunar environment. LADEE met its objectives to successfully create a relatively long baseline of the previously-known species ^{40}Ar, He, Na, and K (Benna et al. 2015a; Colaprete et al. 2016; Hodges and Mahaffy 2016). During the mission, there was also the discovery of CH_4, Ti, Fe, Al, Ca, and Mg (Benna et al. 2015; Colaprete et al. 2015, 2016a,b; Hodges 2016). As discussed in Section 4.1, LADEE also found a strong correlation of exospheric content with the micrometeoroid environment, including the discovery of water release during meteor streams (Benna at al. 2019).

3.1.1.1. Updated inventory. At the time of the LADEE mission formulation, there were about a half-dozen known species in the lunar exosphere (see Table 4.1 of the LADEE Science Definition Team report, 2008, https://lunarscience.arc.nasa.gov/files/LADEE_SDT_Report.pdf). We now count nearly 15 species observed quasi-constantly or released during meteor streams into the exosphere. We also can count at least another 9 complex species from lunar polar crater regions ejected during the transient LCROSS impact event (see Table 2 in Colaprete et al. 2010). Besides these discoveries, the sensitive UV instruments LRO/LAMP and LADEE/UVS have placed upper limits on a range of exospheric species during systematic searches (Cook et al. 2013). We list the known species in Table 1.

3.1.2. The general character of exosphere dynamics. Several processes are responsible for creating and maintaining the lunar exosphere (Stern 1999): thermal desorption, photon-stimulated desorption, charged particle sputtering, and micrometeoroid impact vaporization. The importance of each process depends on the species considered (species that loosely adsorb onto the lunar surface are more likely promoted into the exosphere) and on other factors, such as the time of day (photon-stimulated desorption does not operate at night), temperature, etc.

Mechanisms for losses of exospheric neutrals include photo-ionization (and subsequent entrainment/pick-up by the solar wind magnetic field), electron impact ionization, charge-exchange with solar protons, implantation into the surface, permanent cold-trapping, chemical dissociation of molecules, and gravitational escape. Photo-ionization loss of exospheric neutrals has been observed and monitored by THEMIS-ARTEMIS during periods when the interplanetary magnetic field is directed mostly out of the ecliptic (Halekas et al. 2012b). These and other unique observations of this exospheric loss process are described further in Section 3.3.3.

Killen et al. (2017) presented a general model of exosphere escape, determining the atomic/molecular loss as a function of parent body mass, species mass, and species ejection energy (expressed as temperature). It was found that impact vaporization at ~4000 K at the Moon would eject water molecules from an icy polar surface with about 50% escaping into free space, but the other 50% returning to the surface—to possibly create a water or OH veneer in surrounding locations.

3.1.2.1. Interactions with the surface. All processes that liberate elements into the exosphere, and especially re-emission of previously emitted particles, are affected by *gas–surface interactions*, which are functions of surface composition and space weathering effects.

Table 1. Current inventory of the known native lunar exospheric species. There is an enhancement in the detection of trace species when the surface is energized by meteor streams.

Species	Surface Density or tangent column density:	Sensed by:	Reported by:	Described in:
^{40}Ar	$8 \times 10^4/cm^3$	LADEE NMS	Benna et al. 2015	3.1.6
^{36}Ar	$3 \times 10^3/cm^3$	LACE	Hodges et al. 1974	3.1.1
He	$3 \times 10^4/cm^3$	LADEE NMS	Benna et al. 2015	3.1.4 & 6
Ne	$10^{3-4}/cm^3$	LADEE NMS, LACE	Benna et al. 2015 Killen et al. 2019	3.1.4
Energetic H	~20% of incident SW flux	IBEX, Chandrayaan-1 SARA	McComas et al. 2009; Futaana et al. 2012	3.1.4
H_2	10–50% of incident SW flux	LRO/LAMP	Stern et al. 2013; Hurley et al. 2017	3.1.4
CH_4	$450/cm^3$	LADEE NMS	Hodges 2016	3.1.4
Na	$5 \times 10^9/cm^2$ column	LADEE UVS	Colaprete et al. 2016b	3.1.3 & 5
K	$4 \times 10^8/cm^2$ column	LADEE UVS	Colaprete et al. 2016b	3.1.3 & 5
Ti	TBD*	LADEE UVS	Colaprete et al. 2016a	3.1.5
Fe	TBD*	LADEE UVS/ meteor streams	Colaprete et al. 2015	3.1.5
Al	TBD	LADEE UVS	Colaprete et al. 2015	3.1.5
Ca	TBD*	LADEE UVS/ meteor streams	Colaprete et al. 2015	3.1.5
Mg	TBD	LADEE UVS	Colaprete et al. 2016a	3.1.5
O	$11/cm^3$*	Chandraayaan-1 ENA	Vorburger et al. 2014	3.1.4
OH	TBD*	LADEE UVS/ meteor streams	Colaprete et al. 2015	3.1.5
H_2O	$< 1/cm^3$ nominally, $> 10/cm^3$ during streams	LADEE NMS/ meteor streams	Hodges 2018; Benna et al. 2019	3.1.5 & 4

* Colaprete et al. (2015) ESF report on the brightness change from pre- to post-Geminids meteor shower. The conversion of this brightening into column density values require further analysis. The oxygen density from Vorburger et al. (2014) is only the energetic sputtered component.

A single molecule can bind to the surface via adsorption. Adsorption encompasses both physisorption (weak binding) and chemisorption (strong binding). Physisorption involves the surface binding of an atom or molecule via van der Waals interactions, and for water and other species can be formed by the creation of induced dipole moments at the surface. Since a physisorbed atom is weakly bound, it can be desorbed by thermally exciting internal states or a surface state (Madey et al. 2002).

If the atom is not reflected, any atom returning to the surface likely remains in a physisorbed state a very short time before finding a stronger binding site through surface diffusion. Once an atom finds a deep potential well it becomes chemisorbed, characterized by chemical bonding. The depth of the bonding sites depends on the particular physical state of the surface. Chemisorption sites extend over a wide range with a distribution of adsorption energies characterized by a Weibull distribution. This has been studied extensively for water by temperature programmed desorption (TPD) (e.g., Poston et al. 2015). An important finding from these laboratory studies is that the desorption energy—or more properly the distribution

of binding sites—is highly dependent on the composition of the surface, the grain sizes and the weathering history (Hibbitts et al. 2011; Poston et al. 2013, 2015). For instance, the distribution of binding sites for water on mature anorthositic lunar soil peaks at about 0.7 eV and extends to > 1 eV whereas it only extends to about 0.6 eV in sub-mature low titanium basalt (Poston et al. 2015). Binding energies not only depend on the coordinate along the surface (e.g., top site vs. hollow site) but also on the interatomic distance in the molecule, its orientation with respect to the surface, and individual coordinates of the dissociation products. Thus, the task of obtaining the relevant energies for the chemisorption process is therefore described by a distribution of binding energies representative of these complicated sites (Barrie 2008).

3.1.3. The lunar exosphere's response to the solar radiation. Photon-stimulated desorption (PSD) was first suggested as a source process for the Na exosphere of Mercury by McGrath et al. (1986). By observing the Moon when in the Earth's magnetotail (thus in the absence of driving solar wind), photon-stimulated desorption was found to be a dominant source of exospheric sodium at the Moon (Mendillo and Baumgardner 1995; Mendillo et al. 1999). The PSD cross section was quantified later by laboratory measurements (Yakshinskiy and Madey 1999). Photon-stimulated desorption results from an electron transfer induced by photon bombardment of the surface with energies greater than the threshold value of 3 to 4 eV. PSD only acts on surface-adsorbed Na because photons do not penetrate the bulk of the solid.

Even though sodium is a trace species in the lunar exosphere, its strong doublet D-line fluorescence near 590 nm makes it a bright visible signal to study the PSD process (Potter and Morgan 1988) and, more recently, was monitored for many months in close proximity to the Moon by the LADEE UVS (Colaprete et al. 2016). Figure 3 shows the UVS-measured temporal profile of Na and K during the LADEE mission.

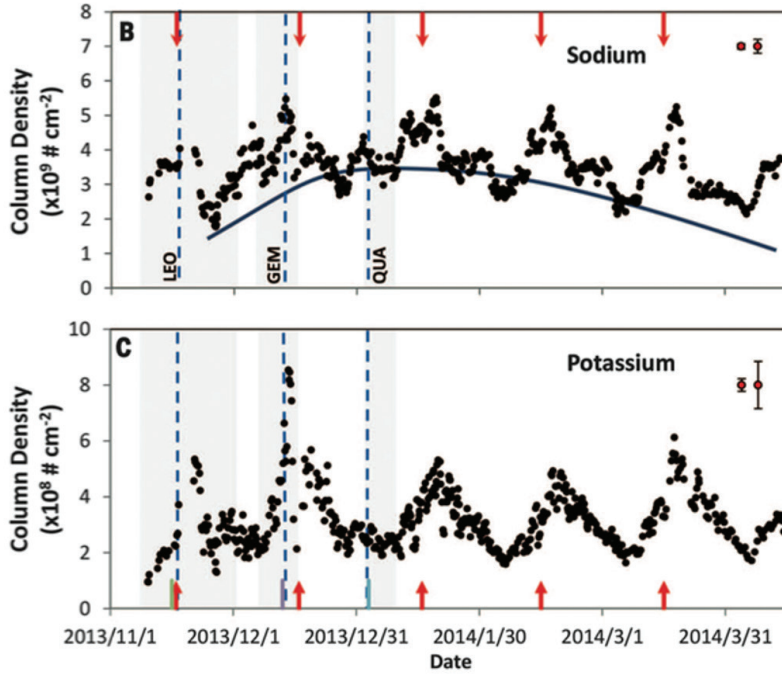

Figure 3. LADEE UVS measurement of exospheric sodium (**top**) and potassium (**bottom**). From Colaprete et al. (2016b). Note that the three **blue dashed lines** are indicative of the Leonids, Geminids, and Quadrantids meteor showers, respectively. The **arrows** indicate full moon.

In the sodium profile in Figure 3 (top), there are two trends: a monthly trend and an overall trend in the baseline. The monthly variation has a dual maximum located at ~20 degrees in ecliptic longitude on either side of full Moon. The overall larger scale trend outlined by the dark line indicates a seasonal effect that was also seen on the LADEE argon profile (Benna et al. 2015) and is likely related to the seasonal exposure of cold traps containing sequestered volatiles (Hodges and Mahaffy 2016). For the potassium profile in Figure 3 (bottom), the peak during each lunation is located when the spacecraft is passing over the KREEP terrain (Colaprete et al. 2016b). Potassium also responded to impact events as well, like the sharp peak found during the incidence of the Geminids stream in December 2013 (see emission maxima at the vertical blue lines).

While photo-stimulated desorption is a source process, photo-ionization and pickup by the solar wind *E*-field represented a loss process for the exosphere. This exospheric loss process is described further in Section 3.3.3 in the discussion of ions of lunar origin.

3.1.4. The lunar exosphere's response to charged particles. In the mid-2000's, the view of the Moon's interaction with the solar wind was that the ions were absorbed and, possibly, were energetic enough upon incidence to sputter regolith atoms into the exosphere with relatively low yields (< 0.1 atoms per ion). The solar wind protons were assumed to 'saturate' the top surface (~200 nm) as implanted hydrogen, although it was never clear what actually happened to these hydrogen atoms over long times. From Apollo LACE observations, neutral helium was found to be a primary constituent in the lunar exosphere. Its correlation with prevailing solar wind momentum flux (see discussion in Stern 1999 and references therein) is indicative of a solar wind He^{++} source. However, LACE operated at night and did not obtain observations in regions of direct solar wind He incidence.

A new view was introduced by Starukhina (2006), who pointed out that the implanted hydrogen is not simply absorbed but rather diffuses into the topmost-surface and is then released as molecular hydrogen—suggesting that the lunar surface is a cycling, dynamic conversion surface and not simply an absorbing boundary. At the time of Starukhina's work, H_2 had not yet been observed in the lunar exosphere (Stern et al. 2012) and hydrogen had not yet been detected in the IR in the lunar soils (Pieters et al. 2009); therefore, these considerations were forward-thinking. As a result of data from LRO, LADEE, Chandrayaan-1, and Kaguya, we now realize that the lunar surface is indeed a conversion surface re-emitting solar wind hydrogen and helium in various forms and with different time constants.

Helium was recently detected by LRO/LAMP (Feldman et al. 2012; Stern et al. 2012; Grava et al. 2016; Hurley et al. 2016) and LADEE/NMS (e.g., Benna et al. 2015a), and is found to be primarily a result of neutralization of solar wind alpha particles. Hurley et al. (2016) integrated a number of data sets, including THEMIS-ARTEMIS solar wind observations, and correlated the helium outgassing to solar wind input flux. In this process, they also identified a quasi-constant background level associated with radiogenic He at about 35% of the total He exospheric content (Fig. 4).

LADEE also detected neon in the exosphere that is suspected to be of solar wind origin (Benna et al. 2015). The densities were comparable to helium, and the species also appeared to behave like a non-condensable gas with peak values over the cold nightside. While the amount of Ne in the solar wind is at trace amounts, its relatively long residence time on the lunar surface is believed to account for its relatively high abundance. Re-examining LACE observations of neon, Killen et al. (2019) reported on surface observations that were an order of magnitude lower than those reported by LADEE. The differing result suggests the possible presence of another neon loss process besides photoionization.

While oxygen makes up close to 50% of the regolith atoms, a direct observation of an oxygen exosphere has eluded detection, with only a lower limit derivable by the LRO LAMP

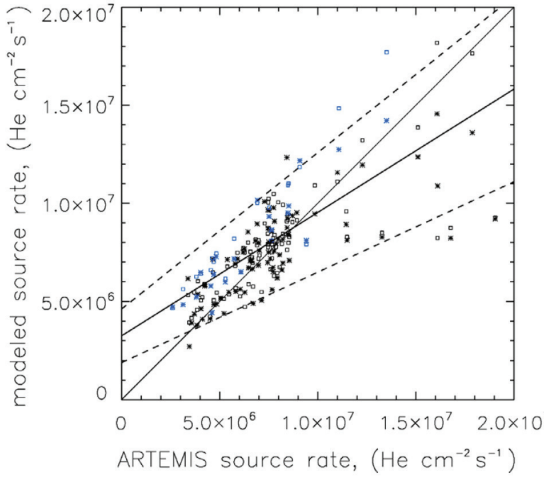

Figure 4. The correlation of helium source rate with driving solar wind rate. The helium exospheric source rate is found to increase directly with the solar wind He^{++} influx. The y-intercept is indicative of the amount of radiogenic helium (more details can be found in Hurley et al. 2016).

observations (Cook et al. 2013). However, using energetic neutral atom sensing, Vorburger et al. (2014) detected energetic sputtered oxygen atoms released from the surface at about 11/cm^3. There may also be a lower energy thermal oxygen component to the lunar exosphere that has yet to be detected.

Regarding solar wind proton-surface interactions, implanted H atoms are now believed to have a very complex set of pathways in the lunar surface. Recent observations suggest that about 1% of the incoming protons are reflected back into the solar wind (Saito et al. 2008), but this reflected ion component can increase to close to 50% over magnetic anomalies (Lue et al. 2011; Poppe et al. 2012a). Incoming protons should charge exchange with the surface (Hodges 2011) and observations suggest that about 20% of the incoming solar wind protons are then re-emitted as energetic neutral H (McComas et al. 2009; Futaana et al. 2012). The surface also re-emits the incident protons in the form of H_2, as predicted by Starukhina (2006), converting about 10–50% of the implanted solar wind proton flux to molecular hydrogen (Stern et al. 2013; Hurley et al. 2017). However, some fraction of the incoming protons may implant and react (at defect sites, etc.) with oxygen atoms in the oxide-rich regolith to form exogenically-created surficial OH (as discussed by Zeller et al. 1966, and more recently observed by Pieters et al. 2009, Sunshine et al. 2009, Clark 2009, and McCord et al. 2011). Recent studies suggest these various implanted-hydrogen pathways may be related to the degree of weathering and solid-state crystal damage of the oxide-rich surface, with even slightly damaged sites delaying hydrogen diffusion in the top 10's of nanometers (Fink et al. 1995; Farrell et al. 2017; Jones et al. 2018; Tucker et al. 2019).

Starukhina (2006) pointed out that implanted H atoms can escape the surface potential barrier by reacting with another H atom to then escape as molecular H_2 via the energy-releasing recombinative desorption process. Jones et al. (2018) pointed out that OH atoms migrating in the regolith can escape the surface as trace amounts of water. However, the discovery of energetic neutral H suggests that there may be other pathways around this surface potential barrier—and the exact process for H escape from the damaged crystal lattice is not fully understood.

Hodges (2016) reported on the LADEE NMS observation of methane-related products in the exosphere, with peak values at dawn having concentrations estimated to be near 450/cm^3. It was proposed that the solar wind implanted H atoms may merge with solar wind implanted

carbon in the diffusion process, thereby creating the more complex molecule (Abell et al. 1971). This observation suggests that the lunar conversion surface is also creating new organic chemistry from the incident atoms in the solar wind, expanding the view of the Starukhina (2006) conversion surface, now to a new complex chemical surface that makes not only H_2 but CH_4 and possibly other species as well. This same conversion and creation of new chemistry may also be active at other airless bodies.

We now know that there is a hydrogen cycle at the Moon, with solar wind H having many pathways out of the conversion-surface. This hydrogen cycle is described more in Section 4.2. The discussion therein places H into the larger lunar water system that also includes the contribution from infalling micrometeoroid material.

3.1.5. The lunar exosphere's response to impactors. Impact vaporization is a universal process at all airless bodies that acts to eject atomic and molecular species into the exosphere. Fast-moving impacting particles of small sizes (< 100 μm) constantly rain onto the Moon's surface at a mean velocity of ~13 km/s (Cintala 1992), churning the regolith, melting, and vaporizing the surface. Pokorný et al. (2019) recently updated the mass flux released via impact vaporization to a value over ten times higher than that in Cintala (1992), at ~10^{-15} g/cm^2·s. Larger meteoroids impact more sporadically, but with higher mean velocity of slightly less than 20 km/s (Marchi et al. 2005). Comets and cometary debris can impact at velocities up to 80 km/s.

Impact events probe to a depth of several diameters of the impacting body and are therefore important in terms of supply of fresh material to the surface, a process referred to as regolith gardening. Because meteoroid impacts probe deeper than any process other than venting, and because the energy density of the process is very high, the exospheric products of this emission process most closely represent the surface composition as a whole (hence, impact vaporization is a stoichiometric process).

As described in Section 4.1, LADEE confirmed the view that micrometeoroid impact vaporization is a dominant process acting on the lunar surface, becoming especially intense during meteoroid streams. As shown in Figure 3, LADEE UVS detected strong micrometeoroid control of both sodium and potassium (Colaprete et al. 2016b) with column densities increasing (many times for K) during incident meteoroid steams (e.g., the Geminids). By merging a set of UVS dawn limb spectra, Colaprete et al. 2015) compared exospheric content pre- and post-Geminids period and found UVS enhancements in oxygen, OH, titanium, iron, aluminum, and calcium in these co-added spectra. The observation of OH raises the question as to whether it is liberated from molecules already in the surface from solar wind production or it is contained in the infalling meteors themselves.

Benna et al. (2019) reported that that the LADEE NMS detected water intensifications at concentrations 2–20 times the background level during meteor streams. The ejected water was believed to result from larger impactors in the stream gardening into a water-rich layer located about 8 cm below the top desiccated soil. These results will be highlighted more in Section 4.1.

3.1.6. The LCROSS impact and transient exosphere. The impact of the LCROSS Centaur booster into Cabeaus crater was at relatively low velocity but relatively high mass impact, thus excavating ~3.5 meters into the surface of the cold polar crater floor (https://www.nasa.gov/mission_pages/LCROSS/searchforwater/LCROSS_impact.html). The corresponding plume of gas and dust from the floor of the permanently shadowed crater was analyzed in both the UV and IR by the LCROSS shepherding spacecraft (Colaprete et al. 2010; Schultz et al. 2010; Ennico et al. 2011), in the UV by LAMP on LRO (Gladstone et al. 2010; Hurley et al. 2012), and in the sodium D-line ~590 nm wavelength by the McMath-Pierce telescope at Kitt Peak ground-based observatory (Killen et al. 2010).

The Centaur impact released 5.6 wt.% of water ice and gas from Cabeaus, and also released over 8 complex compounds from the crater floor, including methane, carbon monoxide,

ammonia, and ethylene—reminiscent of cometary material (see Table 2 of Colaprete et al. 2010; Paige et al. 2010). LRO/LAMP also detected molecular hydrogen, carbon monoxide, calcium, mercury, and magnesium, in the plume. The amount of sodium observed via Kitt Peak ground observations was found to be comparable to the amount of sodium vapor detected by the shepherding spacecraft, and an approximate impact vapor temperature was found to be near ~1000 K (Killen et al. 2010). The results not only provided direct evidence of water and other complex molecules trapped within permanently shadowed regions (PSRs), but also demonstrated a very powerful technique for examining these seemingly inaccessible regions.

3.1.7. The interior's contribution to the lunar exosphere. One of the elements first identified in the lunar exosphere by LACE was ^{40}Ar, which is the product of the radioactive decay of ^{40}K within the lunar crust (Hoffman et al. 1973). This, together with correlation between argon exospheric density and high-frequency teleseismic events (shallow moonquakes) recorded by the Apollo lunar seismic network (Nakamura 1977), revealed that radiogenic gases are being released from the interior of the Moon, through cracks that might be perturbed during moonquakes (Hodges 1977). Interestingly, LACE was located close to circular fault systems (Mare Serenitatis and Mare Tranquillitatis), where deep moonquakes are most likely generated (Runcorn 1974). From the amount of ^{40}Ar leaked into the atmosphere through cracks on the surface it is possible to estimate the amount of the parent ^{40}K within the crust (Hodges and Hoffman 1975). Therefore, any detection of active outgassing has important implications regarding the Moon's formation.

Both LADEE and LRO made inroads in understanding the origin of exospheric sources directly related to the underlying surface. Observations from the LADEE UVS (Colaprete et al. 2016) and the McMath-Pierce telescope in Kitt Peak, Arizona (Rosborough et al. 2019) revealed that potassium emission peaks in the Western hemisphere, in particular near the Oceanus Procellarum and Mare Imbrium, in the area of the KREEP terrain. The LADEE NMS also observed an enhancement of argon also above the Procellarum KREEP Terrane (Jolliff et al. 2000; Benna et al. 2015). By analogy, at Mercury, the exospheric magnesium was also found to be correlated with the underlying composition (Merkel et al. 2018), supporting this similar interior–exosphere connection found at the Moon. In contrast, Killen and Morgan (1993) argued that diffusion of sodium from the interior of Mercury is five orders of magnitude too small to supply sodium to the exosphere, and correctly predicted that the surface abundance of sodium at Mercury is terrestrial-like and not the lunar value. Because diffusion is slower at the Moon than at Mercury, the same argument holds. It can thus be concluded that the source of sodium and potassium at the Moon must then be the surface grains and not the deep interior.

In contrast with sodium and potassium, the source of at least some of the helium is the deep interior of the Moon. For example, Cook and Stern (2014) reported 'helium flares' in LRO/LAMP observations (i.e., unusually high concentration of helium uncorrelated with either solar wind flux or micrometeoroid flux). As describe previously, LRO/LAMP also observed evidence for a portion of the helium exosphere to be of endogenic origin was also presented in Hurley et al. (2016) and Grava et al. (2016) (see Fig. 4 and associated discussion).

3.2. The dust exosphere

Interplanetary dust particles continually bombard all bodies in the Solar System. At our Earth, they produce shooting starts in atmospheres where they typically abate and ionize due to drag heating and rarely reach the ground. In contrast, the IDP flux directly reaching the surface of an airless body can generate impact plumes comprised of a large number of secondary ejecta particles. Impact generated dust exospheres were first observed engulfing the icy moons of Jupiter by the Galileo mission. The Galileo Dust Detector System (DDS) detected enhanced dust densities during the flybys of these moons (Fig. 5), indicating a population of gravitationally bound particles following ballistic orbits (Krivov et al. 2003). Surprisingly, the production of dust ejecta clouds near the moons of Saturn appears to be much less efficient,

especially compared to the copious amount of dust produced in the south-polar geysers on the moon Enceladus (Spahn et al. 2006). The continual IDP bombardment of the Moon was recognized early on as a possibly important process gardening the lunar regolith. However, the dust ejecta cloud generated by the high-speed impacts of IDPs was only recently detected by the LADEE mission (Elphic et al. 2014). The Munich Dust Counter on board the HITEN satellite orbited the Moon from February 15, 1992 to April 10, 1993, but due to its distant orbit and low sensitivity it did not detect the lunar dust ejecta cloud (Iglseder et al. 1996)

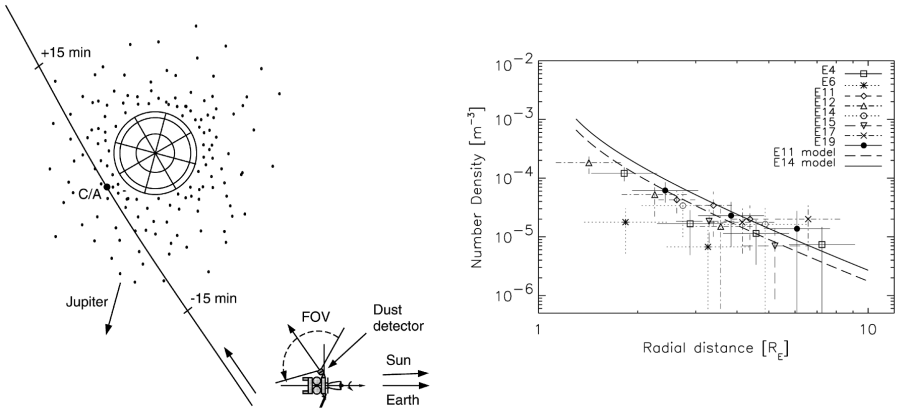

Figure 5. Galileo's trajectory and geometry of dust detection during the E4 Europa flyby. The directions to Jupiter, Earth and Sun are shown. C/A indicates closest approach to Europa (**right**). The number density of dust as a function of distance from the center of Europa, showing the observations (**symbols with error bars**) and the fit (**continuous lines**) using theoretical models (Krivov et al. 2003). Horizontal bars for the data symbols indicate distance bins which were used in processing the data, whereas vertical ones reflect $\sqrt{N}$ errors due to a limited number of impacts (Kruger et al. 2003).

Lunar Ejecta and Meteorites (LEAM) Experiment left by Apollo 17 was designed to detect high-speed incoming meteorites and the secondary ejecta particles they produce (Berg et al. 1974). Instead of the expected rare hits by meteorites, LEAM reported significant dust activity during the passages of the sunrise and sunset terminators, indicating the possible mobilization of highly-charged, slow-moving dust particles (Colwell et al. 2007). An alternate interpretation of the LEAM measurements as possible system noise was suggested by O'Brien (2011). The concurrent rapid temperature changes during LEAM detection periods was suggested to possibly account for the elevated levels of electronics noise in the instrument (Grün and Horányi 2013).

The Moon, unlike Earth, is directly exposed to solar wind plasma and solar ultraviolet (UV) radiation, leading to charging of regolith dust and possible transport (see reviews by Colwell et al. 2007 and O'Brien 2011). Circumstantial evidence of this electrostatic process was the so-called 'lunar horizon glow'. This bright glow has been suggested to be caused by forward scattered sunlight from a cloud of ~10 μm diameter dust particles electrostatically lofted to a height less than 1 m above the surface at the horizon (Criswell 1973; Rennilson and Criswell 1974; Colwell et al. 2007). The electrostatically released fine dust was also suggested to be responsible for high-altitude ray-pattern streamers reported by the Apollo astronauts (McCoy and Criswell 1974; Zook and McCoy 1991). Since then, a number of observations over other airless bodies have been also related to this electrostatic process, such as dust ponds on asteroid Eros and comet 67P (Robinson et al. 2001; Thomas et al. 2015) and radial spokes in Saturn's rings (Smith et al. 1981, 1982; Mitchell et al. 2006). The LADEE lunar dust experiment search for electrostatically ejected small dust to high altitudes, but evidence for such a component could not be confirmed.

3.2.1. LADEE's lunar dust experiment. Prior to the LADEE mission, the lunar dust ejecta cloud had not been confirmed to exist. One of LADEE's primary science objective was to characterize the lunar dust environment. Onboard, it carried the Lunar Dust Experiment (LDEX), an impact ionization dust detector capable of individually detecting grains with radii a > 0.3 μm. The instrument operated by collecting the impact plasma released when high speed (near the LADEE orbital speed) dust grains impacted the LDEX hemispherical target (Horányi et al. 2014). This impact plasma was separated by an imposed electric field and the ion and electron signals were collected for coincidence determination. The minimum detectable size of 0.3 μm in radius (assuming an average dust specific density of 2500 kg/m^3), is set by the minimum detectable signal an impact could generate. The smallest grain that can generate double coincidence measurements, with both an ion and electron signal, is 0.7 μm. While LDEX could not individually detect impacts below 0.3 μm, it had an additional capability to integrate the total impact charge at high cadence to search for the cumulative effect of encountering a large population of submicron dust grains (Horányi et al. 2014).

3.2.1.1. The lunar dust ejecta cloud. The LADEE mission operated at low altitudes (< 260 km) in lunar orbit for approximately 6 months, from October 2013 to April 2014. Throughout the mission LDEX detected approximately 140,000 lunar dust impacts (Horányi et al. 2015; Szalay and Horányi 2015a). Figure 6 shows the LDEX impact rates throughout the entire LADEE mission for both single and double coincidence. As exhibited in this time series, the observed impact rates had significant variations throughout the mission, with notable enhancements during some of the well-catalogued meteoroid showers. With knowledge of the LDEX's boresight vector, effective detector area, and the approximate dust impact velocity, the impact rates can be converted to number densities. The far left panel of Figure 7 shows the average dust density distribution observed by LDEX throughout the mission. Unlike in the Jovian system, the lunar dust cloud is found to be highly asymmetric, with the majority of impact ejecta production occurring on the apex hemisphere. It was determined that the very same sporadic meteoroid sources observed at the Earth (see Section 2.2) cause the observed

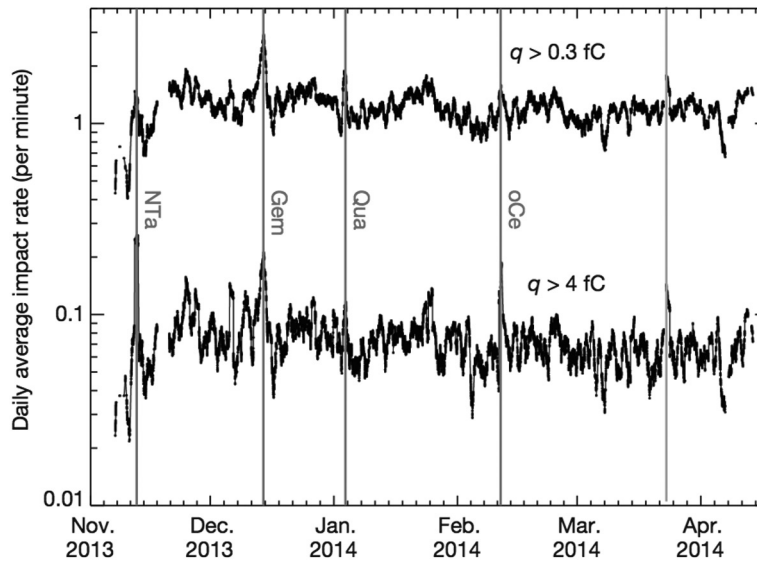

Figure 6. LDEX impact rates for the duration of the LADEE mission. Two size cuts are shown, corresponding to grain radii $a > 0.3$ μm (impact charge $q > 0.3$ fC) and $a > 0.7$ μm ($q > 4$ fC) (Horányi et al. 2015).

impact ejecta cloud structure at the Moon (Szalay and Horányi 2015a). The peak in the apex direction is attributed particularly large impact velocities of the primary sporadic meteoroids generating ejecta, with lunar impact velocities ~60 km/s.

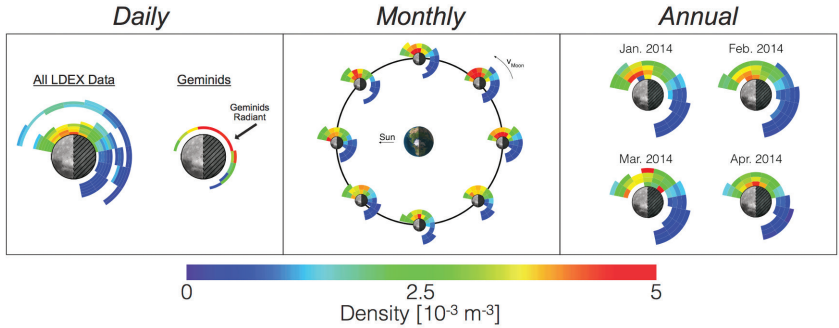

Figure 7. Observed variations in the lunar dust ejecta cloud. The dust cloud exhibited daily variations due to intermittent streams, monthly variations due to the synodic motion of the Moon about the Earth, and observed monthly averaged annual variations throughout the mission.

Additionally, the lunar dust altitude distribution and inferred ejecta velocity distribution was found to differ significantly from the ejecta clouds around the icy Jovian satellites. Unlike the power-law altitude profile observed at Jupiter, the lunar dust cloud scales as an exponential in altitude (Szalay and Horányi 2016b), with an approximate scale height of 200 km. The discrepancy between the power-law altitude distributions observed for the Galilean satellites and the exponential distribution at the Moon could very well be due to separate altitude regimes visited by LADEE and Galileo. With $\hat{r} = r/r_M$, where r_M is the radius of a given moon, LADEE visited a range of $\hat{r} \leq 0.14$, while Galileo visited in the region of $0.13 \leq \hat{r} \leq 8$. Therefore, the two ejecta cloud observations did not measure within the same comparable region. Additionally, the Galileo power law distributions were determined for all four Galilean satellites using a combined total of 141 impacts throughout the Galileo mission. LADEE measured approximately 1,000 times more impacts in its 6 month-long mission, allowing for a significantly more detailed understanding of the impact ejecta environment.

LDEX measurements have revealed a complex and rich ejecta cloud that exhibits temporal variations on timescales of days due to meteoroid showers, weeks from lunar orbital modulation, and months from orbit about the Sun. Figure 7 summarized these variations, which carry key information about the total flux of meteoroids to the Moon and the response of the lunar surface to the impactor distribution. The observations are complementary to ground based optical and radar observations. While ground based observations struggle with the complexity of the ablation processes in the atmosphere, impact generated ejecta production also remains poorly understood. However, the incoming IDP flux at Earth generating shooting stars, and the IDP flux bombarding the Moon generating ejecta clouds are the same, and the combination of these will eventually reveal the true characteristics of the IDP populations near 1 AU.

During several of the well-catalogued meteoroid showers, LDEX observed significant enhancements in the lunar dust ejecta on the hemisphere exposed to these showers. Most notable of these showers was the Geminids, which generated the largest observed enhancement in the lunar dust cloud during the entire LADEE mission. This shower also generated a significant, temporary enhancement in the potassium exosphere (see Fig. 3) (Szalay et al. 2016). Radiant information for this stream (and a few others) was successfully extracted (Szalay and Horányi 2016a). While the extracted radiant parameters do not improve our knowledge of the

directionality of the observed meteoroid streams given their sophisticated ground visual and radar observations of these streams, this result demonstrates a proof-of-concept method to aid in the characterization of meteoroid streams near other airless bodies in the Solar System, without such sophisticated ground networks. Specifically, LDEX-type measurements in the vicinity of the moons Phobos and Deimos could greatly enhance our understanding the dust environment of Mars (e.g., Szalay et al. 2016c), advancing our ability to mitigate the dust hazard for the safety of crew and mission to Mars.

3.2.1.2. High-altitude nano-dust clouds. Apollo 15 and 17 observations of a 'horizon glow' indicated a putative population of high-density small dust particles with radii $\ll 1$ μm near the lunar terminators (McCoy 1976; Zook and McCoy 1991; Glenar et al. 2011). Pre-LADEE predictions (Stubbs et al. 2006) suggested that this high altitude small component might be related to electrostatically-lofted dust inferred from near-surface observations (Criswell 1973; Rennilson and Criswell 1974; Colwell et al. 2007). However, later remote sensing observations from orbit by the Clementine (Glenar et al. 2014) and LRO (Feldman et al. 2014) missions resulted in upper limits on the abundance of such particles a factor of about 10^4 lower than indicated by the Apollo results. The basic characteristics of the lunar dust ejecta cloud have been well observed by the LADEE mission, but the possibly intermittent existence of this dense, small particle cloud at high altitudes still remains a somewhat controversial issue.

LDEX, in addition to detecting single impacts of particles with radii > 0.3 μm, was also capable of measuring the collective signal generated by dust impacts with sizes below its single-particle detection threshold. LDEX performed a dedicated search for the putative population of a high-density nano-particles lofted over the lunar terminator region (Szalay and Horányi 2015b).

Figure 8 shows the LDEX measurements over the lunar sunrise terminator in the altitude range of 3 to 250 km, indicating an upper limit on the submicron dust number density of < 100 m^{-3} while the Moon is in the solar wind, and < 40 m^{-3} during its passage through the Earth's magnetotail, approximately 2–3 orders of magnitude below the expectations based on Apollo observations. Perhaps more telling, the submicron dust density indicated by LDEX remained independent of altitude, rendering the proposed electrostatic mechanisms (Colwell et al. 2007) highly inefficient or incapable of lofting submicron dust particles to high altitudes. However, as discovered in recent laboratory experiments (see discussions in Section 4.3) electrostatic charging, mobilization, and transport of dust particles can be an efficient process close to the surface, well below 3 km, possibly sculpting the distribution of lunar fines on the surface and generating albedo markings ('swirls') in magnetic anomaly regions.

While the LDEX in-situ observations indicated no evidence for high-altitude nano-dust particles, the UVS instrument (Colaprete et al. 2014) onboard the same spacecraft found a fluctuating nano-dust exosphere that is, at least intermittently, dense enough to be detectable via scattered sunlight. Near the peak of the 2014 Quadrantid meteoroid stream, UVS was observing close to the anti-Sun direction when it serendipitously detected a broadband signal consistent with a population of nano-dust grains with radii ≤ 20–30 nm) (Wooden et al. 2016). Subsequently, the LAMP UV spectrograph (Gladstone et al. 2010) on board LRO conducted a search with a geometry closely reproducing the LADEE/UVS measurements in order to observe the backscattered sunlight from lunar exospheric nano-dust particles, especially their anticipated density enhancements during meteoroid stream activity. Figure 8 (right) shows the comparison between the observations by LADEE UVS during the Quandrantid meteoroid shower in 2014, and by the LRO LAMP instrument during the 2016 Quandrantid shower. The observations by LRO LAMP indicate an upper limit that is about 2 orders of magnitude smaller than the nano-dust abundances inferred by the LADEE UVS measurements (Grava et al. 2017). This difference could be due to a number of reasons, including: a) year-to-year variability of the meteoroid shower flux intercepting the Earth–Moon system; b) subtle differences in the observing geometry and instrument performances;

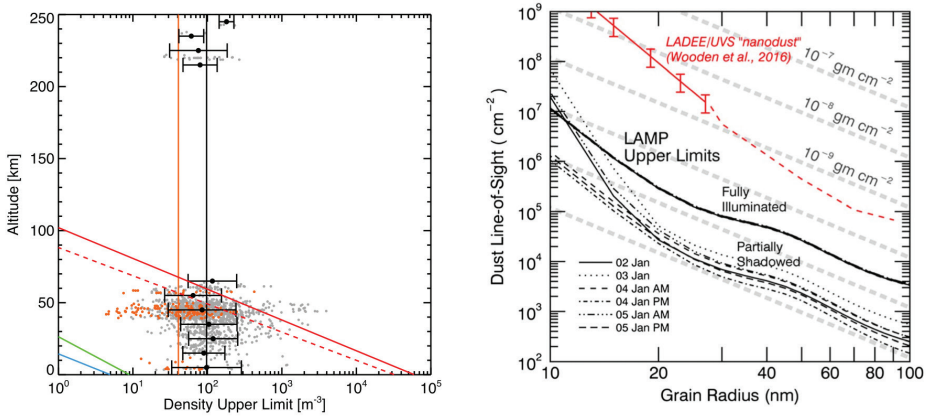

Figure 8. Left: The upper limit on the density of dust particles as a function of altitude, derived from the LDEX current measurements. Each **gray dot** represents a morning terminator crossing. **Black dots** show the averages in 10 km increments. The **orange points** indicate LDEX measurements taken in Earth's magnetotail. The **sloped color lines** indicate the expected nano-dust densities based on Apollo (**red**), Clementine (**green**), and LRO (**blue**) observations (Szalay and Horányi 2015b). **Right**: Upper limits for line-of-sight dust abundance as a function of grain radius, derived from six LRO/LAMP observations (**black lines**) during the period of the Quadrantid meteoroid stream. The **solid red line** shows the LADEE nano-dust estimate (Wooden et al. 2016) during the same meteoroid shower in 2014. The LAMP observations indicate at least 2 orders of magnitude less nanodust during the 2016 Quantrantid shower than inferred by UVS in 2014 (Grava et al. 2017).

c) the solar wind plasma and/or UV conditions resulting in different dust charging environments, influencing the dynamics of nano-dust particles under the influence of the interplanetary magnetic fields (Grava et al. 2017). Hence, the final word on the existence of high-altitude nano-dust particle clouds is yet to be written.

3.2.2. Meteoroid bombardment in the lunar polar regions. While the LDEX measurements were taken near the Moon's equatorial plane, they can be used to infer the impact ejecta environment in the polar regions. This extrapolation is important in understanding the origins and evolution of polar volatiles (e.g., Farrell et al. 2019). As described in this chapter, volatiles experience reduced or completely diminished solar radiation fluxes in the polar regions. However, even Permanently Shadowed Craters will experience continual bombardment by meteoroids, notably those shed from Halley Type Comets that have large inclinations and form the 'toroidal' meteoroid source observed at Earth (Pokorný et al. 2014).

The local time structure of equatorial LDEX impact ejecta measurements were well-explained with a sum of ejecta production from the 4 ecliptic sporadic sources (Szalay and Horányi 2015a). By adding the two high-latitude toroidal sources (NT and ST), a comprehensive full-surface ejecta map can be created (Szalay et al. 2019), shown in the top left panel (a) of Figure 9. The maps are outward viewing Mollweide projections of the expected lunar impact ejecta production in density of ejecta at the surface, n_0. The smaller maps at the top show the ejecta production for the HE and AH, AP, and NT and ST sources, while the larger map that the overall expected ejecta production. As shown here, the NT/ST meteoroid sources are responsible for ejecta production in the high-latitude regions. The top right panel (b) of Figure 9 shows the flux of bound impact ejecta as a function of local time from 0–90˚ latitude, where the ejecta production is assumed to be symmetric about the equator in this model. As shown here, the impact ejecta production is somewhat reduced in the polar regions, yet is still comparable to that in the equatorial region. Even at the lunar poles ±90˚ latitude, a reduction in ejecta production of ~20% is expected and therefore impact bombardment is still able to liberate similar (in order of magnitude) quantities in the high-latitude regions.

Additionally, due to the relatively high speeds of the toroidal source, the polar region is bombarded by fast impactors. The bottom panel of Figure 9 shows the results of using a three-dimensional, dynamical model to predict the impactor distributions incident onto the lunar surface. This panel shows the average meteoroid impact speed as a function of local time and latitude. As shown here, the high latitude regions are exposed to high-speed impactors with ~30 km/s. Even with a somewhat diminished flux at high latitudes, these impactors can still deliver significant energy and deposit heat due to their large impact energies.

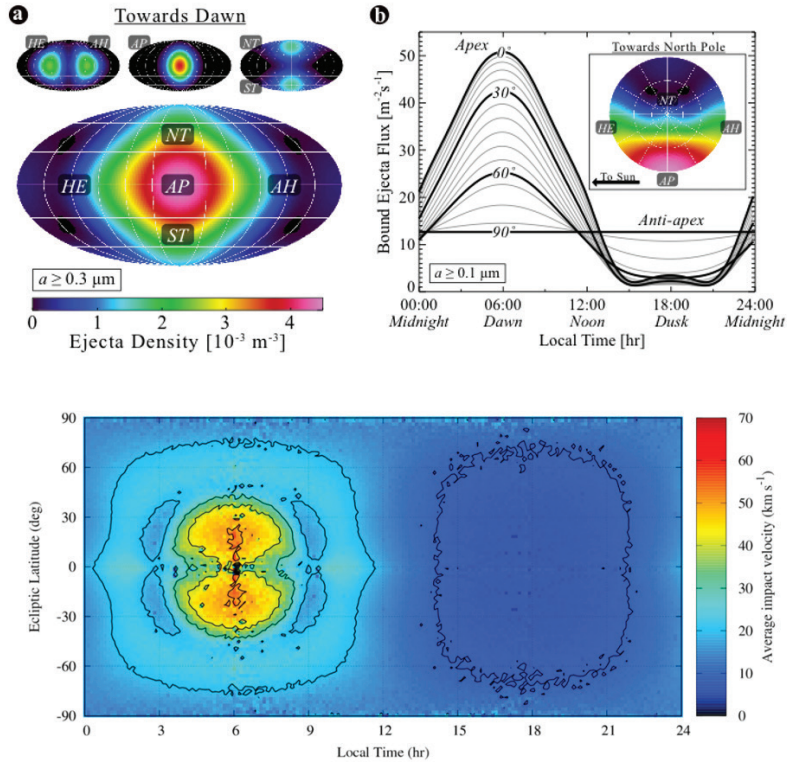

Figure 9. Top: Predicted impact ejecta production over the entire lunar surface (Szalay et al. 2019), reproduced with permission from JGR. **Bottom**: Average impact velocity as a function of ecliptic latitude and local time at the Moon (Pokorný et al. 2019), reproduced with permission from JGR.

An additional consequence of deriving the impact ejecta production over the entire lunar surface is that an estimate of the impact ejecta yield (the ratio of ejecta mass to impactor mass) can be calculated for the Moon in a more robust manner. From both studies that predict the total impact ejecta production at the Moon, the lunar regolith appears to have a very low impact yield on the order of 10 (Pokorný et al. 2019; Szalay et al. 2019). This yield is much lower than yields for Jupiter's icy moons, which had estimated yields in the 10^3–10^4 range, (e.g., Krivov et al. 2003), 2–3 orders of magnitude larger than the lunar yield. This discrepancy could suggest that the fluffy lunar regolith partitions the energy of meteoroid impacts more into heat than to production of ballistic ejecta compared to more solid, icy surfaces. If this is the case, meteoroids may play a more important role in the evolution of volatiles on the lunar surface than previously considered.

3.3. Space plasma interactions

In the past two decades, new measurements from an international fleet of spacecraft including Lunar Prospector (LP), Nozomi, Kaguya, Chandrayaan, Chang'E, THEMIS-ARTEMIS, and LADEE have revolutionized our understanding of the lunar plasma environment. Previously, the Moon was often considered a passive absorber, capable of affecting only a limited region of space. Now we understand that the Moon not only absorbs, but also reflects and emits both neutral and charged particles, resulting in measurable perturbations to the space environment extending many lunar radii from the surface. In turn, the plasma affects the near-surface environment, acting to charge the regolith, producing a trailing wake, serving as a sink and a source for the exosphere, and interacting in a complex fashion with localized remanent magnetic fields.

3.3.1. Global plasma interactions: Dayside interactions. The Moon, with no global magnetic field or collisional atmosphere, lies exposed to the ambient space environment, including charged particles, photons, and micrometeorites. Given the roughness of the surface, one might expect the absorption of incident charged particles after multiple collisions in the upper layers of the regolith, and indeed solar wind proton implantation has significant impacts on the regolith. However, a significant fraction of incoming protons are reflected rather than implanting in the regolith, even in completely unmagnetized regions of the Moon. Ten to twenty percent of incident protons reflect in the form of energetic neutral atoms (ENAs), with energies from a few electron volts (eV) up to the energy of the incident particles (McComas et al. 2009; Wieser et al. 2009; Vorburger et al. 2013), and little or no dependence of the reflection rate on incident flow speed (Futaana et al. 2012, 2013). The reflected ENA energy spectrum has a Maxwellian-like distribution (Futaana et al. 2012), with a high energy tail following a power law (Funsten et al. 2013), and the effective 'temperature' of the distribution proportional to the incident flow speed (Futaana et al. 2012).

A small fraction (~0.1–1%) of the incoming protons reflect from the regolith (Saito et al. 2008, 2010; Lue et al. 2014; Poppe et al. 2017). Results (Lue et al. 2014) suggest a strong dependence of the proton reflection rate on incident flow speed, but recent analyses call this into question suggesting a slight decrease in reflection efficiency at higher speeds (Lue et al. 2018). Reflected protons travel in distinctly different directions from the incoming protons, and therefore respond not only to the interplanetary magnetic field (IMF) but also the motional electric field. The resulting motion (see Fig. 10) has similarities to the cycloidal 'pickup ion' motion followed by ionized neutral particles (Holmström et al. 2010); however, since reflected ions have non-zero initial energy, they can reach velocities up to three times the incident velocity (nine times the incident kinetic energy) (Saito et al. 2010).

The bombardment of the regolith by the solar wind sputters material from the surface (Futaana et al. 2006; Vorburger et al. 2014). The impact of charged particles and solar ultraviolet (UV) photons also leads to the buildup of electrostatic charge on the regolith. Ambient plasmas typically produce a negative current to the surface thanks to the high mobility of electrons, while UV causes photoemission of electrons, producing a competing positive current to the dayside surface. Current balance calculations (Stubbs et al. 2014) therefore predict dayside positive potentials of ~5–10 V for typical conditions. However, particle-in-cell modeling (Poppe and Horányi 2010; Poppe et al. 2011, 2012b) and theoretical calculations (Guernsey and Fu 1970; Grard and Tunaley 1971) predict the existence of non-monotonic potentials above the dayside under some conditions. These structures allow the electrostatic potential of the dayside surface to reach strongly negative values relative to the ambient plasma, though the electrostatic charge on the surface remains positive. In the terrestrial magnetotail, observations from Lunar Prospector (LP) (Halekas et al. 2005a, 2008b, 2012c), THEMIS-ARTEMIS (Halekas et al. 2012b; Poppe et al. 2012b) and SIDE surface package (Collier et al. 2017) have confirmed the existence of non-monotonic potentials, but observations in the solar wind remain more ambiguous (Halekas et al. 2012c).

3.3.2. Global plasma interactions: Trailing plasma wake. Thanks to the absorption or reflection of solar wind plasma on the lunar dayside, a trailing plasma wake forms downstream (see Fig. 10). The structure of the wake depends on solar wind conditions (Ogilvie and Ness 1969; Halekas et al. 2005b), IMF strength and orientation (Colburn et al. 1971; Ogilvie et al. 1996; Halekas et al. 2005b; Holmström et al. 2012; Xu et al. 2019), and the location of crustal magnetic fields (Halekas et al. 2011a). The density gradient across the wake boundary leads to the formation of a diamagnetic current system around the cavity (Colburn et al. 1967; Owen et al. 1996; Fatemi et al. 2013; Vernisse et al. 2013). As a result, the wake contains compressed magnetic fields in the central cavity, surrounded by a rarefaction wave that propagates out into the ambient downstream plasma (Ness et al. 1968; Ogilvie and Ness 1969; Ogilvie et al. 1996; Farrell et al. 1998; Halekas et al. 2005b; Zhang et al. 2014; Xu et al. 2019). Given the supersonic flow of the solar wind, the magnetic field and plasma perturbations in the wake are confined within a Mach cone (Whang and Ness 1970; Fatemi et al. 2013, 2015b), leading to the formation of an additional 'confinement current' at the wake boundary (Whang and Ness 1970; Fatemi et al. 2013, 2015b). Using 6 years of THEMIS-ARTEMIS data, Xu et al. (2019) compared the statistically-derived potential, *E*-field, and magnetic configuration of the lunar wake to expansion models for comparison and contrast—representing the most complete study of the downstream region to date.

When a thermal plasma expands across a plasma-vacuum interface like the wake boundary, the difference in electron and ion mobility leads to the formation of an electrostatic potential that accelerates ions into the vacuum (Gurevich et al. 1969). However, the lunar wake's small size, the non-thermal particle distributions in the solar wind and magnetosheath, and the effects of the IMF complicate its refilling (Halekas et al. 2014b). The wake refills not only through plasma expansion along the magnetic field (Ogilvie et al. 1996; Birch and

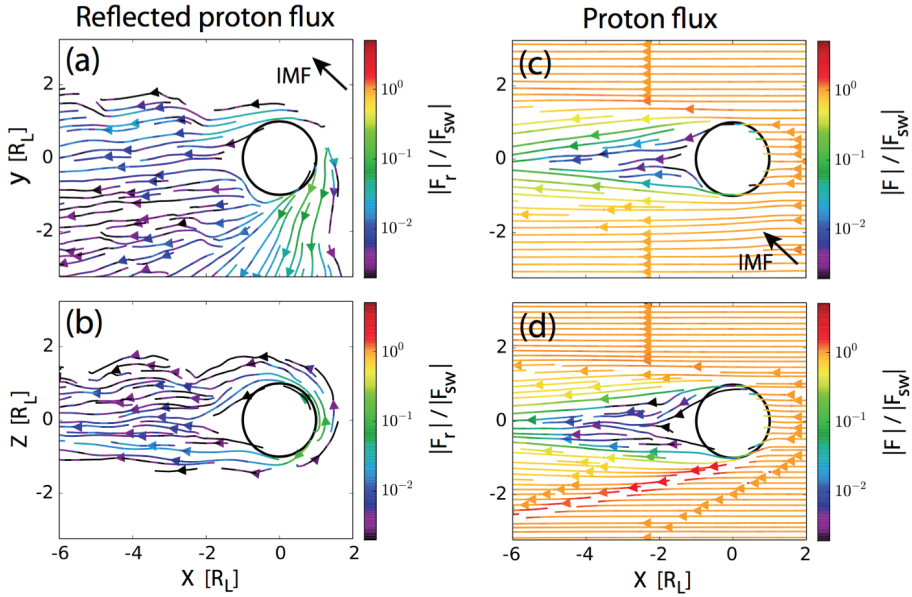

Figure 10. Global interaction of the solar wind with the Moon, including reflected protons from the surface and crustal magnetic fields, after Fatemi et al. (2014). Panels show streamlines of particle velocity for **(a,b)** reflected protons and **(c,d)** all protons in the plane containing the IMF **(a,c)** and the plane perpendicular to the IMF **(b,d)**, with **colors** indicating the normalized flux relative to the incident solar wind.

Chapman 2001a,b; Futaana et al. 2001, 2003; Nishino et al. 2009a), but also through fluid convection (Wiehle et al. 2011; Zhang et al. 2012, 2014; Halekas et al. 2014b), particle gyromotion (Nishino et al. 2009b; Fatemi et al. 2012), and ion reflection from the lunar dayside (reflected ions have gyro-radii comparable to the lunar radius and can enter the wake) (Nishino et al. 2009b, 2010; Futaana et al. 2010; Wang et al. 2010a; Fatemi et al. 2014), and from the terrestrial bow shock (Nishino et al. 2017).

Though the lunar wake contains only very tenuous plasma, the nightside surface will charge strongly negative, with electrons typically providing the primary charging current. Electrons in the wake can have much higher temperatures than in the ambient solar wind thanks to velocity filtration across the wake boundary (e.g., Halekas et al. 2005b), leading to a commensurate increase in the surface potential. LP observed surface potentials on the order of −200 V near the edges of the lunar wake, with less negative potentials relative to the plasma near the center of the wake (Halekas et al. 2008b), possibly due to the increase in secondary electron emission with electron temperature (Halekas et al. 2008b, 2009a).

3.3.3. Global plasma interactions: Ions of lunar origin. Measurements of ionized species derived from the Moon provide a sensitive probe of the exosphere and surface (Hartle and Killen 2006), with lunar ions measured from the surface (Benson et al. 1975), in orbit (Tanaka et al. 2009; Yokota et al. 2009, 2014; Saito et al. 2010; Wang et al. 2011a; Halekas et al. 2012b, 2013a, 2015, 2016; Poppe et al. 2012c, 2016a), and at more distant locations (Hilchenbach et al. 1991, 1993; Mall et al. 1998). Detections or inferred detections include H_2^+, He^+, C^+, O^+, Ne^+, Na^+, Al^+, $CO^+/Si^+/N_2^+$, K^+, Ar^+/Ca^+, and Fe^+. Measurements vary widely, and disagreement persists as to the most common ion species, in part due to the different observation geometries, but also due to ambiguity as to the source of the ions.

As described previously in Section 3.1.2, ions around the Moon originate both from ionization of exospheric constituents and directly from the surface (Tanaka et al. 2009; Yokota et al. 2009), with the bombardment of the regolith by solar photons, solar wind ions, and interplanetary dust capable of stimulating the emission of both ions and neutral particles (Elphic et al. 1991; Madey et al. 1998). A significant portion of the Na^+ and K^+ fluxes measured near the Moon likely originate from photon-stimulated desorption and solar wind sputtering from the surface, both in neutral and charged form, and they have a dawn–dusk asymmetry that reflects the diurnal variation of both sources and sinks of Na and K on the lunar surface (Yokota et al. 2014).

On the other hand, LADEE, which made observations sensitive only to low-energy ions produced locally in the exosphere, found the highest fluxes (in order) for $CO^+/Si^+/N_2^+$, Ar^+/Ca^+, O^+, and Ne^+ (see Fig. 11) (Halekas et al. 2015). The Ar^+ and Ne^+ signals appear consistent with neutral composition data that reveal high abundances of the noble gases (Benna et al. 2015). However, the dominant peak at 28 amu remains puzzling, with CO^+ apparently the most plausible species (note that neutral CO is difficult to measure due to instrumental backgrounds). CO has no selenogenic source, implying a solar wind and/or micrometeoritic origin. Since CO can photodissociate to form O^+ and C^+, its presence may help explain the surprising detections of those two species (also observed by other lunar missions), otherwise difficult to reconcile with spectroscopic limits (Stern 1999; Cook et al. 2013).

As discussed above, non-monotonic potentials can form above the lunar dayside, creating a local potential well on the order of the ambient Debye length (~10 m in the solar wind and ~1 km in the terrestrial magnetotail lobes). While photo-ions created above this well are accelerated towards the surface (Collier et al. 2017), those created within the well should be trapped, and simulations suggest that the buildup of these ions should remove the non-monotonic structure (Campanell and Umansky 2016). The observable presence of non-monotonic potentials may therefore indicate that trapped ions escape the well before destabilizing the non-monotonic potential structure, possibly via particle drifts or fluctuations in the sheath structure.

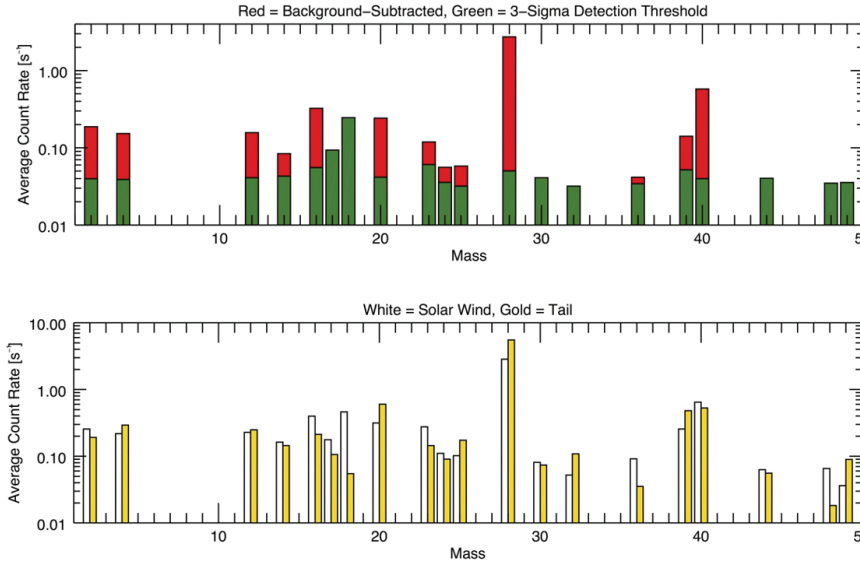

Figure 11. Lunar exospheric ions measured by LADEE, after Halekas et al. (2015). The **top panel** shows background-subtracted rates in comparison to background (**bars with red** visible represent statistically significant detections), and the **bottom panel** compares raw solar wind and magnetotail count rates.

3.3.4. Regional plasma interactions and microphysics: Magnetic anomaly regions. In contrast to the low levels of charged particle reflection from the unmagnetized regolith, up to ~50% of the incident solar wind proton flux can reflect from strong lunar crustal magnetic fields (Hood et al. 2001; Saito et al. 2010; Wieser et al. 2010; Lue et al. 2011; Deca and Divin 2016; Poppe et al. 2017). This high reflection rate implies at least partial shielding of the surface in more strongly magnetized regions, and may affect the space weathering of the surface, potentially explaining the unique albedo signatures observed in association with lunar magnetic fields. Given the small scale of the crustal fields in comparison to relevant plasma scales, electric fields generated by differential motion of ions and electrons above the magnetized areas are required to efficiently reflect such a large fraction of the solar wind (Lue et al. 2011; Saito et al. 2012; Deca et al. 2014, 2015; Jarvinen et al. 2014; Poppe et al. 2014a; Fatemi et al. 2015a). Confirming this hypothesis, Kaguya observed simultaneous deceleration of solar wind ions and acceleration of solar wind electrons at ~25 km altitude over magnetic anomalies (Saito et al. 2012), with the correspondence between the deceleration energy/charge for both H^+ and He^{++} and the acceleration energy for electrons indicating the existence of strong quasi-static upward electric fields at low altitudes in magnetic anomalies. Deca et al. (2018) presented a comprehensive 3-D kinetic plasma simulation at the Reiner Gamma anomaly using the Surface Vector Mapping magnetic expansion from Tsunakawa et al. (2015) showing this solar wind 'standoff' effect. In addition, Chandrayaan imaged the associated electrostatic potential in one magnetic anomaly region (Fig. 12), utilizing the speed dependence of the distribution of energetic neutral atoms scattered from the surface to infer surface potentials (Futaana et al. 2013). The two complementary techniques both infer an electrostatic potential increase on the order of ~150 V inside magnetic anomalies.

At higher altitudes, intermittent enhancements in magnetic field magnitude, often associated with plasma compression and deflection, occur near the outer boundary of the lunar wake (Siscoe et al. 1969; Barnes et al. 1971; Sonett and Mihalov 1972; Russell and Lichtenstein 1975). These 'limb shocks' or 'limb compressions' are closely associated with crustal magnetic fields (Mihalov et al. 1971; Lin et al. 1998; Halekas et al. 2008a), but can have much larger scales than the crustal sources themselves and extend to large distances (multiple

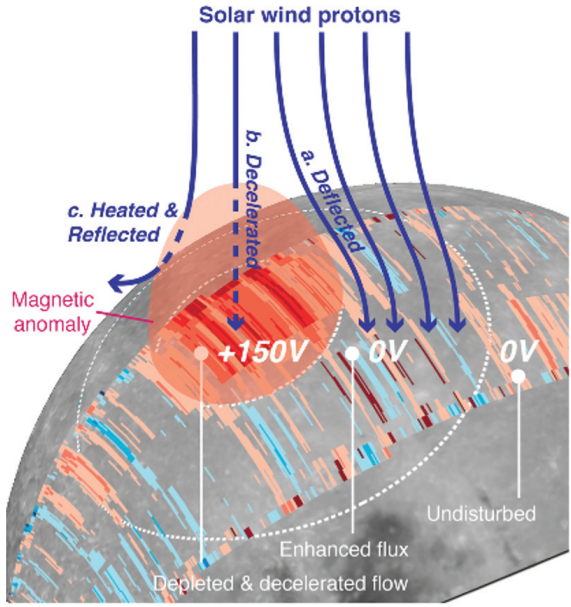

Figure 12. Surface electrostatic potential near the Gerasimovich magnetic anomaly, as derived from Chandrayaan-1 energetic neutral atom measurements, after Futaana et al. (2013).

lunar radii) downstream from the Moon. Though small in scale compared to planetary bow shocks, these structures share many of the characteristics of collisionless shocks, including compression, heating, dissipation in the form of plasma waves, and deceleration and deflection of the plasma flow across a discontinuity (Halekas et al. 2014a). The interaction between incoming solar wind protons and the reflected proton population appears responsible for forming these structures (Fatemi et al. 2014), possibly due to momentum exchange between reflected protons and the incident solar wind (Halekas et al. 2017).

3.3.5. Regional plasma interactions and microphysics: Localized electric fields at shadow boundaries. At the lunar terminator (including the poles), the solar wind flows nearly horizontally over the surface. Local topography can obstruct or block solar wind plasma entry to form localized mini-wakes, which also initiate the start of the larger trailing plasma void/wake region, as examined in detail via analytical modeling and particle-in-cell plasma simulations (Farrell et al. 2008, 2010; Jackson et al. 2011; Zimmerman et al. 2011, 2012, 2013). Simulations of the inflow into polar craters predict the development of a standing plasma double layer over and around local terminator and polar topographic features (Zimmerman et al. 2011), with this layer controlling the ion and electron flux to the crater floors (Farrell et al. 2013, 2015; Zimmerman et al. 2013). Applications of these plasma influx models have been made to human system charging (astronaut, rovers), which is relevant to exploration, especially the charging and discharging of human systems in shadowed, plasma-depleted regions (Zimmerman et al. 2012; Jackson et al. 2015). In addition, plasma sputtering of ice from crater floors may prove comparable to meteoric vaporization in driving losses of surface volatiles in polar cold traps (Farrell et al. 2015).

Away from the terminator, surface topography and roughness on both macroscopic and single grain scales may perturb the local electrostatic environment. Simulations indicate that decimeter sized craters could significantly influence the lunar photoelectron sheath, leading to negative surface potentials and enhanced electric field strengths on the lee side of the crater (Poppe et al. 2012d; Piquette and Horányi 2017). These enhanced fields may play a role in the

mobilization of dust grains near the lunar terminator (Collier et al. 2013). Similarly, complex electrostatic fields may exist within lunar pits due to the close proximity of sunlit photoemitting surfaces with neighboring shadowed surfaces (e.g., Haruyama et al. 2009; Robinson et al. 2012; Miyake and Nishino 2015).

On small grain-level scales, it has been shown that exposure to either UV photons or energetic electrons can generate electric fields strong enough to mobilize dust grains with radii on the order of tens of microns, as demonstrated in the laboratory (Wang et al. 2009, 2010b, 2011b). Experiments and theory suggest a 'patched charge model' to explain how individual micron-sized dust grains can charge on microscales to build up anomalously large (i.e., much larger than the local Debye sheath electric field strength) electric fields that result in ballistic dust motion (Wang et al. 2016a; Zimmerman et al. 2016). The laboratory study of the charge-heterogeneous surface and subsequent grain ejection is described in more detail in Section 4.3.

3.3.6. Regional plasma interactions and microphysics: Precursor effects and plasma instabilities. Though the region far upstream from the Moon is typically not strongly affected by the solar wind interaction with the lunar surface, the 'fore-moon' and 'fore-wake' regions encompassing magnetic field lines that pass through the Moon and its wake contain a wide variety of plasma waves and modified plasma distributions (Bale et al. 1997; Nakagawa et al. 2003; Halekas et al. 2012a, 2013b). The interaction of ambient plasma with the Moon naturally creates reflected and newly created ion and electron populations that are unstable (Fig. 13), leading to the formation of an extended region of plasma waves and turbulence (Harada et al. 2015; Harada and Halekas 2016; Luo et al. 2016) both upstream on Moon-connected field lines and in the trailing lunar wake. Some of the observed waves occur only under very specific plasma conditions, providing a unique view into the dynamic microphysics that governs the near-Moon plasma environment.

As discussed above, a small percentage of solar wind protons reflects from unmagnetized regions, and a much larger fraction reflects from magnetized regions. As a result, both narrowband and broadband whistler-mode waves with frequencies on the order of 1 Hz occur regularly near the Moon (and particularly near strong crustal magnetic sources) (Halekas et al. 2006; Nakagawa et al. 2011; Tsugawa et al. 2011, 2012, 2014, 2015). Narrowband ULF waves with frequencies on the order of 0.01 Hz also occur in the same regions, with surface reflected protons again a likely source (Nakagawa et al. 2012). As discussed above, reflected

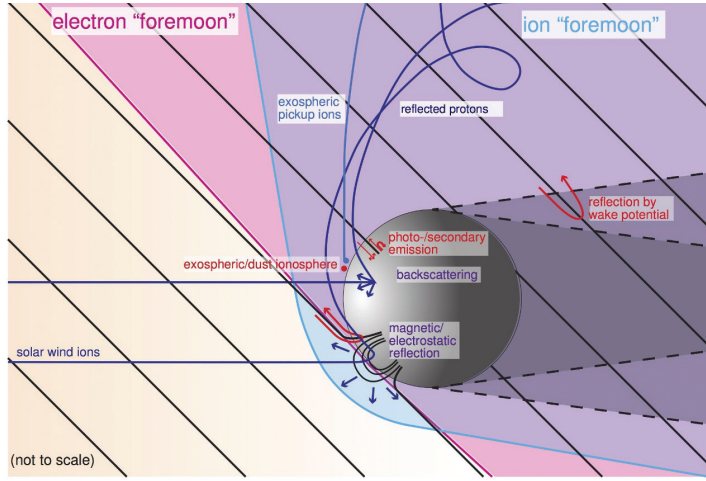

Figure 13. Sources of precursor effects and plasma instabilities in the lunar environment, after Harada and Halekas (2016).

protons can also lead to the formation of plasma compressions and even potentially small-scale shocks, which can locally generate a variety of waves (Halekas et al. 2014a).

The presence of the Moon also naturally creates electron velocity distributions with free energy that can drive instabilities, leading to the growth of a wide range of plasma waves and further modifications of upstream electron distributions. Though most incident electrons are absorbed by the lunar regolith, some fraction of incident electrons backscatter from the surface. Photoelectron emission from the lunar dayside also produces an electron population that can drive instabilities. Electrons that reflect from magnetic fields, meanwhile, have a 'loss cone' distribution that can drive higher-frequency whistler-mode waves (Harada et al. 2014).

When reflected protons gyrate into the lunar wake, they form a highly unstable distribution that drives a range of wave activity (Nishino et al. 2010; Nakagawa et al. 2015). The entry of ions and electrons along field lines, meanwhile, creates unstable distributions subject to streaming instabilities that can produce electrostatic waves (Farrell et al. 1997, 1998; Hashimoto et al. 2010; Halekas et al. 2011b; Hutchinson 2012; Tao et al. 2012).

3.3.7. Special plasma environments. When the Moon passes through the region of space affected by the Earth, it encounters radically different plasma conditions from the solar wind. When the solar wind meets the obstacle formed by Earth's magnetic field, a bow shock forms and the plasma flow is slowed, heated, and deflected around the Earth. Upstream from the shock, reflected ions back-stream along magnetic field lines in the 'foreshock' and can affect the Moon and its near-surface environment (Collier et al. 2011; Nishino et al. 2017). At the bow shock, the presence of the Moon perturbs the current system and deforms the shock surface (Nishino et al. 2011). In the magnetosheath, high plasma pressure from heated ions leads to dramatically enhanced magnetic fields in the central wake (Poppe et al. 2014b). In the magnetotail lobes, the flow is sub-magnetosonic and lunar plasma dominates (Tanaka et al. 2009; Poppe et al. 2012c; Zhou et al. 2013), leading to dramatic changes in the lunar environment (Harada et al. 2013; Zhou et al. 2014). In the central plasmasheet, energetic plasma bombards the surface and can charge it to kilovolt negative potentials (Halekas et al. 2005a, 2011b; Poppe et al. 2011). On the other hand, in the low-density magnetotail lobes, observations indicate that the dayside lunar surface can reach potentials of +40–200 V (Tanaka et al. 2009; Poppe et al. 2012c), with these large positive potentials generated by the high energy tail of photoelectrons emitted from the lunar surface (Harada et al. 2017). In the low density magnetotail, the Moon represents a significant source of charged particles, which travel along magnetic field lines and can even reach the Earth, with some particles observed to reflect from the Earth's dipolar magnetic field and return to the Moon (Halekas et al. 2011b), while others may impact the terrestrial atmosphere. Conversely, the Moon serves as a sink for terrestrial plasma, which can flow out from the terrestrial ionosphere and reach the Moon (Poppe et al. 2016b; Terada et al. 2017), depositing terrestrial material in the regolith. Unique plasma instabilities occur in the magnetotail, with ULF wave activity generated by plasmasheet ions and/or lunar ions (Halekas et al. 2012a; Chi et al. 2013, Nakagawa et al. 2018), and both broadband electrostatic emissions and electron cyclotron harmonics associated with upgoing electron beams produced by surface charging (Poppe et al. 2012b).

The lunar plasma environment also responds dramatically to solar events. Coronal mass ejections, solar energetic particle events, and other types of solar impulses can not only deliver dramatically higher fluxes of charged particles but can impact the surface with plasma of different composition and energy than quiescent solar wind. The lunar dayside may respond to the impact of more energetic plasma, particularly if it includes a significant heavy ion component (with higher sputtering efficiency, see Hayderer at al. 2001; Kracher et al. 2003, Barghouty et al. 2011), by releasing more material into the exosphere (Killen et al. 2012). Meanwhile, the night side responds strongly to energetic particles, which freely access the low-density wake thanks to their large gyro-radii, leading to dramatically increased negative surface potentials of up to 4 kilovolts (Halekas et al. 2007, 2009b, 2011a; Farrell et al. 2012).

In summary, in the last 10 years, our understanding of the lunar space plasma environment has made great leaps. The twin THEMIS-ARTEMIS spacecraft have been in the near-vicinity of the Moon providing new observations of the exo-ionosphere and deep plasma wake region. Kaguya provided unique perspectives of the near-Moon region including the discovery of reflected protons, *E*-fields in magnetic anomalies, and unusual wake configurations. These new findings expand our knowledge provided by the Lunar Prospector and ALSEP plasma packages. The new frontier is now to obtain new plasma measurements directly on the surface, like in nightside region, within polar craters and within magnetic anomalies.

4. NEW TOPICS AND ADVANCES

Since the mid-2000's there have been a number of advancements in the topic of dust, atmosphere, and plasma that are highlighted further in this section. These advancements typically merge concepts from other areas including elements of surface volatiles and space weathering.

4.1. LADEE and the renewed appreciation of meteoric control of the exosphere

Prior to the LADEE mission, there were numerous ground-based and spacecraft measurement campaigns to study the lunar exospheric sodium and potassium distributions and their influences by the space environment (plasma and impacts) (e.g., Sprague et al. 1992; Potter and Morgan 1994; Verani et al. 1998; Smith et al. 1999; Potter et al. 2000; Kagitani et al. 2010; Tenishev et al. 2013). Additionally, modeling efforts continue to unravel the complex interplays between the exospheric sources and sinks (Sarantos et al. 2010, 2012). Amongst the many features of the lunar exosphere these studies illuminated, there is the provocative observation via ground-based observatories of an exospheric response during the Leonids and Taurids meteoroid showers (Verani et al. 1998; Smith et al. 1999). However, ground-based measurements to date had yet to uncover exospheric profile throughout a full lunar cycle.

The LADEE mission was able to make high resolution, continuous measurements of many lunar exospheric constituents (Colaprete et al. 2016). Notably, LADEE was also uniquely equipped to investigate the importance of meteoroid bombardment on exospheric neutral generation as it had both UVS (Colaprete et al. 2014) to measure exospheric populations and LDEX (Horányi et al. 2014) to quantify particulate ejecta from instantaneous meteoroid input.

For example, during the Geminids meteor shower, a large enhancement of exospheric potassium was observed (see Fig. 3). The K enhancement persisted for a longer duration than the meteoroid input and, using a simple decay model, a lunar potassium decay constant of 4–8 days was found to be consistent with these observations. With the exception of the Geminids, the large enhancements in the observed exospheric potassium were well correlated with the surface K concentration (Colaprete et al. 2016), indicating the potassium source regions on the lunar surface play an important role in their lifecycle.

Further punctuating the meteor-exosphere connection, Benna et al. (2019) reported on the presence of water in the LADEE NMS during meteor streams. They examined periods when the NMS was first turned on, to avoid water-contaminating effects on the background by the warm instrument. During instrument 'off' periods, they found that water had collected on the interior walls of the open source chamber and these 'cold-collection' time-integrated water levels correlated with meteoric activity on the lunar surface activity. Figure 14 shows the observation of the cold-collected water (collected while the NMS was turned off and cold) during the Geminids shower. Benna et al. suggest that the NMS-detected water originates from the lunar surface as a result of heavy impactors in the stream penetrating into a water-rich layer about 8 cm below a dry regolith. They further suggested that exospheric water release during nominal times did not occur because the lower energy sporadic impactors do not penetrate the desiccated layer to the underlying water-rich layer.

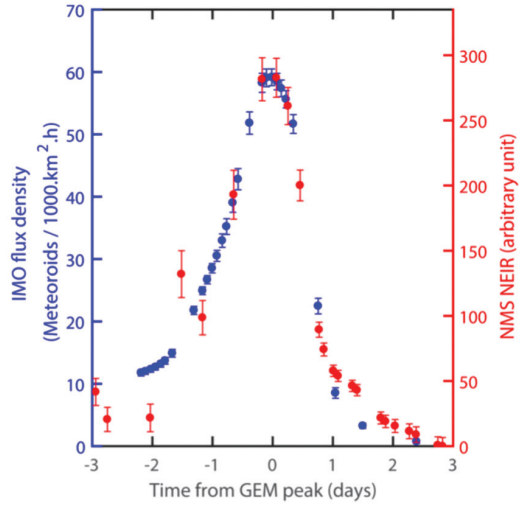

Figure 14. LADEE NMS observations of normalized water levels and of Geminids meteoric influx activity (Benna et al. 2019).

4.2. The hydrogen and water cycles

The Moon contains far more hydrogen and OH than previously believed at the time of the first NVM edition in 2006. Figure 15 shows the various dynamic, modern (i.e., ongoing) sources that contribute to lunar surface hydrogenation, hydroxylation, and possible hydration in regions away from polar craters. These sources include the delivery of volatiles via a continual stream of micrometeoroids (Morgan and Shemansky 1991; McCord et al. 2012; Hurley et al. 2017), solar wind implantation with possible hydroxylation and hydration (Starukhina 2006; Farrell et al. 2015, 2017; Jones et al. 2018; Tucker et al. 2019), infall of ejected volatiles originating from the distant polar cold trap reservoirs (Farrell et al. 2015b), and volatile emission by space weathering from now-exposed internal mantle minerals at pyroclastic deposits and at some magmatic-originating crater central peaks (Klima et al. 2013; Milliken and Li 2017). The space environmental damage to the surface via plasma and impact processes creates crystal defects and unsatisfied chemical bonds in the crystal that further enhance the trapping and chemical alteration of the sorbed or implanted hydrogen, OH, and water—the damage is thus self-fortifying in retaining H species (Starukhina 2006; Dyar et al. 2010; Jones et al. 2018; Tucker et al. 2019). As illustrated in Figure 15 and described previously in Section 3.1.4, the solar wind ion's interaction with the lunar regolith leads to H-species release back into the exosphere as energetic protons, energetic neutral H, H_2, methane, and possibly water. The solar wind-surface interaction represents a sub-cycle to the overall lunar water system. The lunar surface does not simply absorb the solar wind protons, but processes and re-emits them in other forms. The interface is thus a hydrogen chemical conversion surface.

This solar wind subsystem is one element in a larger lunar water system, and it remains unclear how these various components shown in Figure 15 interconnect. While it was initially believed that the 3-micron IR signature resulted from solar wind (Sunshine et al. 2009; McCord et al. 2011), the observation of water by LADEE during meteoroid streams possibly suggests meteoric infall as a release process that might account for part of the IR surface observations (Hurley and Benna 2017; Benna et al. 2019). LRO/LAMP also reported on the possible signature of surface water on the lunar dayside, with the water displaying a diurnal effect in the UV analysis (i.e., LAMP-observed water levels reduced as the surface warms) (Hendrix et al. 2012, 2019).

However, the LAMP-observed water release in warm regions should create exospheric water levels that would have been easily detectable by the LADEE NMS (as a water exosphere at > 100/cm^3). Such a high density water exosphere was not detected (Hendrix et al. 2019). The LADEE NMS provided a lower limit to the water exospheric density (in non-meteor stream periods) of less than 1/cm^3 (Hodges 2018; Benna et al. 2019). Thus, there remains inconsistencies in the water measurements made between remote and in situ sensing assets.

Another possibility shown in Figure 15 for the mid-latitude water is that it is ejected from the polar crater floors via micrometeoroids and sputtering in those polar regions (Farrell et al. 2013, 2015). However, that expected flux is not high enough to account for the observed OH signature at 10–1000 ppm.

Finally, it remains unclear if the solar wind hydrogen, OH, and water system at lunar mid-latitudes is connected to the hydrogen in the polar cold traps. A key question is whether water molecules can migrate from location to location via the adsorption/desorption process to find their way to the poles (e.g., Crider and Vondrak 2000). It may be that water simply hops once—from its origin to another location—to then be dissociated upon contact at the hop landing location. If this one-hop scenario is the case, the mid-latitude water may not find its way to the polar cold traps. In this case, the modern mid-latitude water system would not be connected to the reservoir trap.

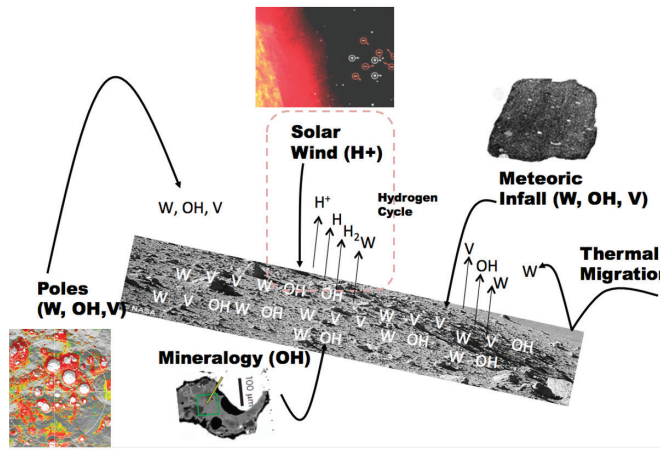

Figure 15. An illustration of the lunar water and hydrogen cycle for mid-latitude regions. W= Water, OH = Hydroxyl, V = Volatile.

The polar reservoir, itself, has been suggested to be an ancient signature of water associated with polar wander (Siegler et al. 2016) and thus may not receive any substantial inflow from modern transport processes. If so, it would suggest the reservoir is not a renewable resource. In contrast, if water can find its way to the poles and meteoroids create regolith turnover at 10's of centimeter scales in polar craters, the modern migrating water from midlatitude might find its way to the poles and then mix with the reservoir material, allowing an exchange of modern and past water deposits. This kind of connection of the modern water system to the paleo-reservoir may only become apparent with a future landed mission to polar regions that assesses the volatile dynamics within the permanently shadowed craters.

4.3. Laboratory studies of dust, plasma, and exosphere formation

4.3.1. Dust charging and transport on regolith surfaces. There has been much effort in the laboratory to understand the physics behind electrostatic processes shaping the dust

distribution on the surfaces of airless planetary bodies, including the Moon. As described in Section 3.2, levitated dust at the terminator has been suggested as an explanation for the lunar horizon glow observed by Surveyor (e.g., Fig. 16, left) (Criswell 1973; Rennilson and Criswell 1974; Colwell et al. 2007). In fact, dust shedding, spreading, and levitating above surfaces in various plasmas have been demonstrated and studied in laboratory (Sheridan et al. 1992; Sickafoose et al. 2002; Flanagan and Goree 2006; Wang et al. 2009, 2010b, 2011b; Hartzell et al. 2013). However, LADEE did not detect such lofted grains at high altitudes (Horányi et al. 2015; Szalay and Horányi 2015b).

Despite the possibility of charged dust lofting/levitating, it remains poorly understood how such dust particles residing on the surface could obtain sufficiently large charge states to be lofted or mobilized. The charge of individual dust particles on a smooth surface (Wang et al. 2007) and the surface charge density on a dusty surface (Ding et al. 2013) in plasmas have been measured but found that these charge levels are too small to mobilize, lift or loft individual dust particles from the surface.

However, recently, new laboratory experiments (Wang et al. 2016a; Schwan et al. 2017) have fundamentally advanced our understanding of dust charging and transport on the regolith surfaces. Micron-sized dust particles (both individuals and aggregates) have been lofted to several centimeters above the surface by exposure to UV light or plasmas (Fig. 16). The equivalent maximum height on the lunar surface was ~12 cm that is comparable to the height (<1 m) of the lunar horizon glow.

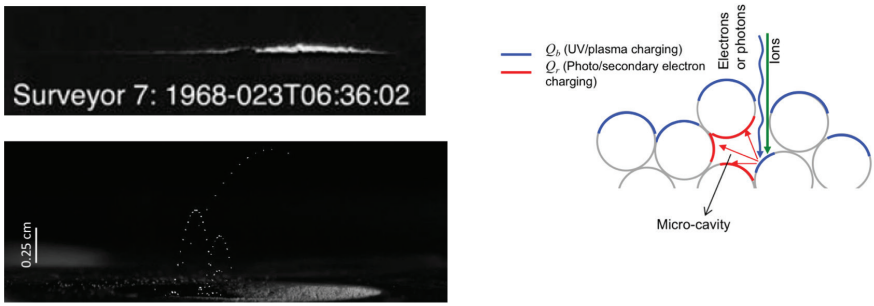

Figure 16. Image of the Lunar horizon glow taken by the Surveyor spacecraft on the lunar surface (**top left**). Hopping trajectories of dust particles exposed to 120 eV electrons in a laboratory experiment (**bottom left**). A sketch of the patched charge model indicating the role of porosity in regolith charging (**right**), from Wang et al. (2016a).

Previous charging theories (Flanagan and Goree 2006; Sheridan and Hayes 2011; Heijmans and Nijdam 2016) only considered the charging process on the top surfaces (blue patches shown in Fig. 16) of dust particles, which are directly exposed to UV or plasma. However, a dusty surface has a unique difference from a smooth surface: micro-cavities are formed between neighboring dust particles and intense *E*-fields can form in these cavities. A new 'patched charge model' has been developed (Wang et al. 2016a). Figure 16 illustrates the model. UV photons and/or electrons and ions can go through small openings in the top surface layer to illuminate surface patches of the dust particles underneath. These patches emit photo and/or secondary electrons. A fraction of these emitted electrons will be absorbed inside micro-cavities and deposit negative charges on the surrounding surfaces (red patches).

The electric field inside the cavity (at the red patches) is very large due to the close grain-grain separation, inter-grain charging, and capacitive effects in comparison to the electric field on the surface (at the blue patches) This buildup of charge and *E*-field within the

cavity increases the electrical stresses and results in an impulsive release of grains. This new model was later verified with the measurements of the dust charge state (Schwan et al. 2017). It shows that: (1) all lofted dust particles are charged negatively even under UV radiation; (2) these lofted negative charges are orders of magnitude larger than the charges predicted from previous charging models. The large repulsive forces between these negative charges are suspected to eject dust off the surface. These new laboratory results will help us to ultimately resolve the unexplained space observations and, more importantly, to understand the role of electrostatic dust transport in shaping the surfaces of the Moon and other airless bodies.

4.3.2. ***Laboratory studies of the plasma sheath above the lunar surface.*** As described in Section 3.3.1, on the dayside, the surface is charged to a few volts positive with respect to the ambient because the photoelectron flux emitted from the surface dominates over the incoming solar wind electron and ion fluxes. On the nightside, a plasma wake is formed and thermal electrons will charge the surface to be negative. Sheath formation on the dayside lunar surface has been theoretically investigated (Nitter et al. 1998; Poppe and Horányi 2010; Poppe et al. 2012b). Hobbs and Wesson (1967) developed the first fundamental model that describes a sheath solution for the case that electrons are emitted from a planar surface in a plasma that consists of cold ions and Maxwellian electrons. In the lab, Wang et al. (2016b) increased the ratio of the secondary electron flux to the primary electron fluxes from a surface and examined the profile of the surface potential. Figure 17 shows a transition of the sheath profile from the classical monotonic, space-charge-limited (SCL) transition (the electric field at the surface is zero) to SCL non-monotonic sheaths. These experimental results show a good agreement with the theoretical prediction by Hobbs and Wesson (1967). All these works indicate that the sheath dynamics on the dayside lunar surface can be significantly changed both temporally and spatially, depending on the ratio of the photoelectron to incoming electron fluxes.

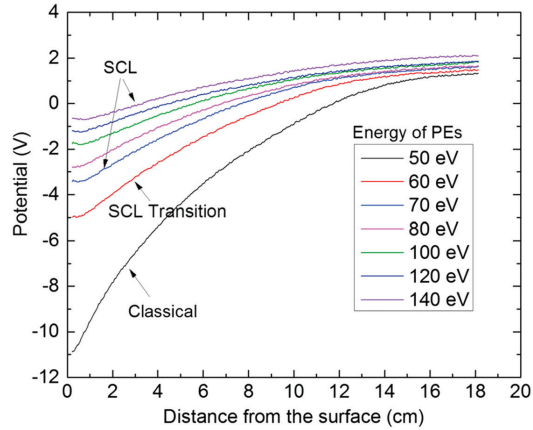

Figure 17. Plasma sheaths above an electron-emitting surface. The ratio of the secondary electron to primary electron (PE) fluxes is increased with an increase in the energy of PEs hitting the surface (Wang et al. 2016b).

4.3.3. Laboratory experiments on the solar wind plasma interaction with surface magnetic anomalies. Also described in Section 3.3.1 are lunar magnetic anomalies that have been found to significantly influence the incoming solar wind. While in-situ observations and computer simulations mainly investigate this interaction at higher altitudes, laboratory studies are able to assess the electrical environment on the surface in the magnetic anomaly regions. Figure 18 shows the formation of mini-magnetospheres in the laboratory experiments

(Bamford et al. 2012). It has also been shown that the large variations in the surface charging in the dipole field regions are due to charge separation on the surface (Wang et al. 2012, 2013; Howes et al. 2015). In the regions where the electrons are magnetically shielded, the surface is charged by unmagnetized solar wind ions to a potential much more positive than the generally expected few volts positive due to photoemission (Howes et al. 2015). This result is also indicated from the observation of a +150 V potential on the surface in the Gerasimovic magnetic anomaly region (Futaana et al. 2013). The large positive surface potentials may alter the solar wind ions impinging the surface and therefore change the space weathering effect. Also, the surface electric fields in these regions may result in lofted charged dust particles, partially responsible for the formation of 'lunar swirls' (Garrick-Bethell et al. 2011).

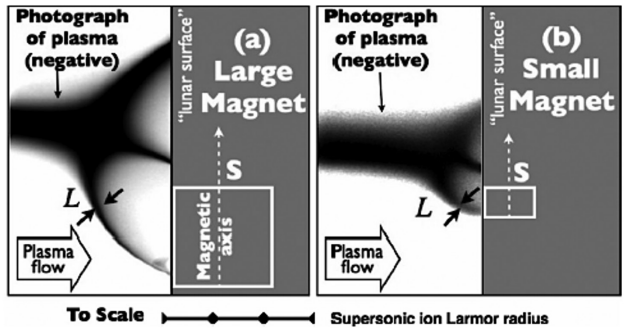

Figure 18. Photographs of the supersonic plasma stream being deflected by two different strength magnets (Bamford et al. 2012).

4.3.4. Temperature Programmed Desorption (TPD) laboratory studies. Neutral atoms and molecules in the surface-bounded exosphere, like argon and water, may adsorb onto the lunar surface and remain trapped in the inter-atomic potential that is established between the atom and the surface regolith. This regolith surface is itself damaged—riddled with defects and vitrified—due to space weathering processes like solar wind implantation and sputtering, micrometeoroid vaporization and subsequent condensation (Dyer et al. 2010).

In the last decade, a set of new laboratory experiments have been run to enhance our understanding of the water sorption properties on weather regolith. These are Temperature Programmed Desorption (TPD) experiments that dose a sample with a known surficial water content and then observed the associated water desorption as a function of increasing temperature (Hibbitts et al. 2011; Poston et al. 2013, 2015). The results verify that water binding to the weathered lunar regolith from mature highlands cannot be described by a single binding energy, but instead by a distribution of binding energy with some activated site with energy above 1 eV (Poston et al. 2015). It was found that up to 10% of the exposed surface of the mature highland sample has these anomalously high water molecule trapping sites, suggesting that the weathered regolith can trap water even at temperatures above 200 K.

5. FUTURE DIRECTIONS AND CONCLUSIONS

There are a number of exciting new avenues for further investigation of the dust, atmosphere, and plasma environments at the Moon. We examine these opportunities herein.

5.1. Cubesat missions

Over the last decade, the 'CubeSat paradigm', a technology for rapid, low-cost development of compact spacecraft utilizing standardized deployers and subsystems to support

a variety of payloads, has evolved considerably from its original vision as an educational and experimental platform for use in low Earth orbit only. As capabilities have grown, the emerging vision now includes multi-platform fleets to provide distributed sensors and thus multi-point measurements of dynamic processes and platforms useful for rapid, low-cost deep space qualification of emerging technologies that utilize and share launch services. Many concepts that range from focused pathfinders to multi-platform projects have been developed for deep space missions and, in particular, for lunar science.

CubeSat missions, deployed from orbiters or landers acting as carriers, have been proposed for a variety of venues including environments of special interest on the Moon, such as the polar regions, terminator-crossings, and inside and near magnetic anomalies. Lunar Flashlight, LunaH-Map (Lunar Polar Hydrogen Orbiter), Lunar IceCube, and SkyFire are all slated to fly as secondary payloads on the SLS Artemis-1 mission. These four missions are specifically designed to provide greater understanding of the distribution, sources, sinks, and processes for lunar volatiles. While each of these Artemis-1 cubesat missions were selected independently, as a group they all complement each other and can be considered a lunar volatile science fleet. We note that Lunar Flashlight was later removed from the Artemis-1 manifest and flew on a separate launch.

Lunar IceCube utilizes a broadband (1–4 μm) Infrared (IR) Point Spectrometer, a compact version of OSIRIS REx (Origins, Spectral Interpretation, Resource Identification, Security, Regolith Explorer) OVIRS (OSIRIS-Rex Visible and InfraRed Spectrometer). The goal is to place the cubesat spectrometer in a highly elliptical, nearly polar, equatorial periapsis orbit, to detect absorption bands of components of water in various states as a function of time of day, latitude, and geomorphology. Both Lunar Flashlight and LunaH-Map will fly in highly elliptical, polar periapsis orbits, with instruments designed to detect ice near the poles. LunaH-Map utilizes a neutron spectrometer to measure variations in neutron flux associated with the presence of hydrogen to a depth of one meter. Lunar Flashlight uses a laser to induce reflectance at two wavelengths associated with ice absorption. A returned reflectance signal decreased by absorption will indicate the presence of surface ice. Finally, SkyFire will investigate the thermophysical properties of the lunar regolith including variations in the distribution, size, and abundance of its components with a thermal IR detector.

Although not nominally targeting science objectives, both the Japanese and Europeans have lunar CubeSats in development to launch on NASA's Artemis 1 mission. JAXA will contribute a semi-hard impactor called OMOTENASHI (Outstanding Moon exploration Technologies demonstrated by Nano Semi-Hard Impactor). OMOTENASHI will deploy a mini lunar lander weighing about a kilogram. In addition, ESA is supplying ArgoMoon, a CubeSat that will provide vehicle operations information through photography.

5.2. Polar volatile exploration from orbit and the surface

From polar orbit, dust detection measurements could yield valuable information about the volatile content in the polar regions. Impact ejecta may contain a signature of the surficial volatile distribution from its ejection site. As previously discussed, a polar orbiting spacecraft equipped with a dust detector would detect a substantial number of impacts from the polar regions. With a refined version of the dust detector LDEX onboard LADEE, with an added impact ionization mass spectrometer feature, these ejecta measurements could reveal compositional information about the measured dust grains. Specifically, surficial water could potentially be detected by an orbiting dust detector, allowing in-situ impact ejecta measurements providing key insights on the surface polar volatiles (Szalay et al. 2019).

Additionally, these measurements can be directly mapped back to the lunar surface. The resolution of tracing the ejected grains back to the surface would depend partially on the altitude of the spacecraft, but for typical orbits with altitudes of ~100 km, impacts could be

traced back to surface patches with ~10's km precision. If such an orbiter flew through a dense ejecta plume (for which LADEE flew through many, see Szalay and Horányi 2016b and Bernardoni et al. 2019), these impacts would be able to be traced back to the surface with single km-scale resolution.

An exciting upcoming mission to examine the surface and subsurface polar volatiles is the Volatiles Investigating Polar Exploration Rover (VIPER) (see https://www.nasa.gov/viper/overview). In a south polar region near Nobile crater, VIPER will characterize the nature of surface and subsurface water (and other volatiles) to determine their origin and distribution. This information will feed forward to create more optimized methods for harvesting such polar resources. VIPER will feature a neutron spectrometer to measure subsurface hydrogen levels, along with a near IR/visual spectrometer and a mass spectrometer for molecular sensing. The rover will also carry a 1-m drill. These instruments will work in tight coordination to determine the water distribution down to 1 meter, along with the drill sample's overall volatile content. A key objective will be to determine the volatile content heterogeneity in both the areal and vertical dimensions at local scales. The VIPER results will thus have a large impact on future resource prospecting and extraction scenarios.

5.3. Surface measurements within non-polar special regions

As described in Section 3.3, swirl magnetic anomalies are special regions where solar wind influx and energy to the surface is reduced, while micrometeoroid influx remains constant. The bright regions are likely connected to regions of reduced solar wind inflow that also lack a strong surface hydroxylation signature (Kramer et al. 2011).

To understand the solar wind-surface interaction in high B regions, it would be desirable to land a magnetoplasma sensing system, Quasi-DC *E*-field sensing system, and an IR system to sense the OH signature near 3 microns. Landing in two regions would be ideal: one where the magnetic field is vertical and directly connected to the solar wind and a second where the B field is horizontal and ambipolar *E*-fields may slow the plasma.

To garner further understanding on these regions, NASA recently selected Lunar Vertex to place an operational lander and rover within the Reiner Gamma magnetic anomaly (Blewett et al. 2022). The lander will include a set magnetometers and a plasma spectrometer while the rover will carry a multispectral microscope and magnetometer. This pioneering mission will provide first-ever near-surface measurements of the effect of the solar wind-surface interactions within magnetic anomalies.

Another region of both scientific and exploration interest is the lunar terminator. It is near the terminator where the LEAM experiment, placed on the Moon during the Apollo 17 mission, possibly detected low energy dust events (Berg et al. 1976). The terminator region is also rich in plasma physics effects due to the solar wind's interaction with the Moon. Such effects include plasma density anomalies associated with plasma expansion into the vacuum region behind the Moon and the formation of ambipolar electric fields and double layers (e.g., Crow et al. 1975; Samir et al. 1983; Farrell et al. 1998, 2002, 2008; Zimmerman et al. 2011). These anomalous plasma structures may be the reason for local terminator dust lifting/lofting observed by LEAM and the Surveyor cameras. A measurement set includes a magnetoplasma sensing system, quasi-DC *E*-field system, and slow dust detection system.

5.4. Networks

A necessary prerequisite for the complete characterization of dust, atmosphere, and plasma at the lunar surface is the development of concepts for low-cost, compact packaging for several in-situ instruments that are deployable on a lander deck and capable of stand-alone operation during lunar day as well as lunar night.

Ideally, these landers would be in a distributed network, to simultaneously acquire measurements at polar to equatorial latitudes and at several times of day on the surface, hopefully complemented by in orbit measurements. These instruments would make both environmental and geophysical measurements and include magnetometers, particle analyzers, electric field instruments, volatile sensors (IR, mass spectrometer) as well as compact seismometers and retroreflector arrays. Thus, proposed lunar geophysical networks could also incorporate environmental sensors to measure dust, atmosphere, and plasma space weather at the surface.

5.5. Summary

The last decade has been an explosive time for exploration of the dust, atmosphere, and plasma environment at the Moon. New missions have obtained unique observations of the complex lunar environment. The system is driven by external energy in the inner heliosphere (electromagnetic radiation, plasma, and meteoroids) and the surface response to these drivers is the creation of a secondary dust flux, the formation of the exosphere, and alterations on the near-surface plasma flow. The next ten years will feature landed missions making use of both NASA resources and also engaging with the new and exciting commercial ventures that will provide more frequent access to the Moon. As an example, NASA has created the Commercial Lunar Payload Services (CLPS) initiative where companies are paid a fee to deliver payloads to the lunar surface. Both VIPER and Lunar-Vertex are part of the CLPS program. Under CLPS, it is anticipated that two lunar missions will fly per year.

In the future, we can envision the study of the lunar volatile and dust system in a similar manner as is currently done in the study of the Earth's weather: With orbital reconnaissance obtaining the context and ground-based systems getting validating local measurements. For example, small volatile-measuring stations could be dropped as a volatile network in a ring around the poles and along certain predefined longitudes to monitor the flow of volatiles locally and to examine the heterogeneity in that flow. Infrared sensors could examine the local surface for changes in volatile retention while UV sensors would look up to quantify the content of the migrating volatiles and dust. Ion mass analyzers would measure in-situ the local volatiles at ground level. These surface systems would provide ground measurements that complement the remote sensing orbiting volatile monitor that is examining the regional/hemispheric dynamics. One can even envision a dynamic map of the lunar dust, atmosphere, and plasma weather, with remote sensing observations overlaid on local ground reports—much like the modern weather reports for Earth.

REFERENCES

Abell PI, Cadogan PH, Eglinton G, Maxwell JR, Pillinger CT (1971) Survey of lunar carbon compounds. I. The presence of indigenous gases and hydrolysable carbon compounds in Apollo 11 and Apollo 12 samples. Proc 2nd Lunar Planet Sci Conf 2:1843–1863

Bale SD, Owen CJ, Bougeret JL, Goetz K, Kellogg PJ, Lin RP, Manning R, Monson SJ (1997) Evidence of currents and unstable particle distributions in an extended region around the lunar wake. Geophys Res Lett 24:1427–1430

Bamford RA, Kellett B, Bradford WJ, Norberg C, Thornton A, Gibson KJ, Crawford IA, Silva, L, Gargaté L, Bingham R (2012) Minimagnetospheres above the lunar surface and the formation of lunar swirls. Phys Rev Lett 109:081101

Barghouty AF, Meyer FW, Harris PR, Adams JH Jr (2011) Solar-wind protons and heavy ions sputtering of lunar surface materials. Nucl Instrum Methods Phys Res B 269:1310–1315

Barnes A, Cassen P, Mihalov JD, Eviatar A (1971) Permanent lunar surface magnetism and its deflection of the solar wind. Science 172:716–718

Barrie PJ (2008) Analysis of temperature programmed desorption (TPD) data for the characterisation of catalysts containing a distribution of adsorption sites. Phys Chem Chem Phys 10:1688–1696

Benna M, Mahaffy PR, Halekas JS, Elphic RC, Delory GT (2015a) Variability of helium, neon, and argon in the lunar exosphere as observed by the LADEE NMS instrument. Geophys Res Lett 42:3723–3729

Benna M, Hurley DM, Stubbs TJ, Mahaffy PR, Elphic RC (2015b) Observations of meteoroidal water in the lunar exosphere by the LADEE NMS instrument, LPI Contrib 1863:2059

Benna M, Hurley DM, Stubbs TJ, Mahaffy PR, Elphic RC (2019) Lunar soil hydration constrained by exospheric water liberated by meteoric impacts, Nat Geosci 12:333–338
Benson J, Freeman JW, Hills HK (1975) The lunar terminator ionosphere. 6th Proc Lunar Sci Conf 3013–3021
Berg OE, Richardson FF, Rhee JW, Auer S (1974) Preliminary results of a cosmic dust experiment on the Moon. Geophys Res Lett 1:289–290
Berg OE, Wolf H, Rhee JW (1976) Lunar soil movement registered by the Apollo 17 cosmic dust experiment. *In:* Interplanetary Dust and Zodiacal Light. Elsässer H, Fechtig H (eds) Springer-Verlag, Berlin, p 233–237
Bernardoni EA, Szalay JR, Horányi M (2019) Impact ejecta plumes at the Moon. Geophys Res Lett 46:534–543
Birch PC, Chapman SC (2001a) Particle-in-cell simulations of the lunar wake with high phase space resolution. Geophys Res Lett 28:219
Birch PC, Chapman SC (2001b) Detailed structure and dynamics in particle-in-cell simulations of the lunar wake. Phys Plasmas 8:4551–4559
Blewett, DT, Halekas, J, Ho GC, et al. (2022) Lunar Vertex: Prism-1a Project Status. Lunar Exploration Analysis Group Abstract 5009, LPI Contrib. No. 2696
Brault J (1972) Kitt Peak Solar Atlas, Kitt Peak Observatory
Campanell MD, Umansky MV (2016) Strongly emitting surfaces unable to float below plasma potential. Phys Rev Lett 116:085003
Campbell-Brown M (2008) High resolution radiant distribution and orbits of sporadic radar meteoroids. Icarus 196:144–163
Chi PJ, Russell CT, Wei HY, Farrell WM (2013) Observations of narrowband ion cyclotron waves on the surface of the Moon in the terrestrial magnetotail. Planet Space Sci 89:21–28
Cintala MJ (1992) Impact-induced thermal effects in the lunar and Mercurian regoliths. J Geophys Res Planets 97:947–973
Clark RN (2009) Detection of adsorbed water and hydroxyl on the Moon. Science 326:562
Colaprete A, Schultz P, Heldmann J, Wooden D, Shirley M, Ennico K, Hermalyn B, Marshall W, Ricco A, Elphic RC, Goldstein D, Summy D, Bart GD, Asphaug E, Korycansky D, Landis D, Sollitt L (2010) Detection of water in the LCROSS ejecta plume. Science 330:463–468
Colaprete A, Vargo K, Shirley M, Landis D, Wooden D, Karcz J, Hermalyn B, Cook A (2014) An overview of the LADEE ultraviolet-visible spectrometer. Space Sci Rev 185:63–91
Colaprete A, Sarantos M, Shirley M, Vargo K, Cook A, Wooden DH, Hermalyn B, Landis D, Karcz B (2015) An Examination of LADEE UVS Spectral Variability Associated with the Geminid Meteoroid Shower. NASA Exploration Science Forum, Moffett Field, CA, July 21–23 2015
Colaprete A, Wooden D, Cook A, Shirley DH, Sarantos M (2016a) Observations of titanium, aluminum and magnesium in the lunar exosphere by LADEE UVS. NASA Exploration Science Forum, Moffett Field, CA, July 20–22 2016
Colaprete A, Sarantos M, Wooden DH, Stubbs TJ, Cook AM, Shirley M (2016b) How surface composition and meteoroid impacts mediate sodium and potassium in the lunar exosphere. Science 351:249–252
Colburn DS, Currie RG, Mihalov JD, Sonett CP (1967) Diamagnetic solar-wind cavity discovered behind Moon. Science 158:1040–1042
Colburn DS, Mihalov JD, Sonett CP (1971) Magnetic observations of the lunar cavity. J Geophys Res 76:2940–2957
Collier MR, Hills HK, Stubbs TJ, Halekas JS, Delory GT, Espley J, Farrell WM, Freeman JW, Vondrak RR (2011) Lunar surface electric potential changes associated with traversals through the Earth's foreshock. Planet Space Sci 59:1727–1743
Collier MR, Farrell WM, Stubbs TJ (2013) The lunar dust pendulum. Adv Space Res 52:251–261
Collier MR, Newheart A, Poppe AR, Hills HK, Farrell WM (2017) Stair-step particle flux spectra on the lunar surface: Evidence for nonmonotonic potentials? Geophys Res Lett 44:79–87
Colwell JE, Batiste S, Horányi M, Robertson SR, Sture S (2007) Lunar surface: Dust dynamics and regolith mechanics. Rev Geophys 45:RG2006
Cook JC, Stern SA (2014) Sporadic increases in lunar atmospheric helium detected by LAMP. Icarus 236:48–55
Cook JC, Stern SA, Feldman PD, Gladstone GR, Retherford KD, Tsang CC (2013) New upper limits on numerous atmospheric species in the native lunar atmosphere. Icarus 225:681–687
Crider DH, Vondrak RR (2000) The solar wind as a possible source of lunar polar hydrogen deposits. J Geophys Res 105(E11):26773–26782
Criswell DR (1973) Horizon-glow and the motion of lunar dust. *In*: Photon and Particle Interactions with Surfaces in Space. Grard RJL (ed) Springer, New York, p 545–556
Crow JE, Auer PL, Allen JE (1975) The expansion of plasma into a vacuum. J Plasma Phys 14:65
Deca J, Divin A (2016) Reflected charged particle populations around dipolar lunar magnetic anomalies. Astrophys J 829:60
Deca J, Divin A, Lapenta G, Lembège B, Markidis S, Horányi M (2014) Electromagnetic particle-in-cell simulations of the solar wind interaction with lunar magnetic anomalies. Phys Rev Lett 112:151102
Deca J, Divin A, Lembège B, Horányi M, Markidis S, Lapenta G (2015) General mechanism and dynamics of the solar wind interaction with lunar magnetic anomalies from 3D PIC simulations. J Geophys Res 120:6443–6463
Deca J, Divin A, Lue C, Ahmadi T, Horányi M (2018) Reiner gamma albedo features reproduced by modeling solar wind standoff. Commun Phys 1:12

Denevi BW, Noble SK, Christoffersen R, Thompson MS, Glotch TD, Blewett DT, Garrick-Bethell I, Gillis-Davis JJ, Greenhagen BT, Hendrix AR, Hurley DM, Keller LP, Kramer GY, Trang D (2023) Space weathering at the Moon. Rev Mineral Geochem 89:611–650

Ding N, Wang J, Polansky J (2013) Measurement of dust charging on a lunar regolith simulant surface. IEEE Trans Plasma Sci 41:3498–3504

Domingue DL, Chapman CR, Killen RM, Zurbuchen TH, Gilbert JA, Sarantos M, Benna M, Slavin JA, Schriver D, Trávníček PM, Orlando TM (2014) Mercury's weather-beaten surface: Understanding Mercury in the context of lunar and asteroidal space weathering studies. Space Sci Rev 181:121–214

Dyar MD, Hibbitts CA, Orlando TM (2010) Mechanisms for incorporation of hydrogen in and on the terrestrial planetary surfaces. Icarus 208:425–437

Elphic RC, Funsten HO III, Barraclough BL, McComas DJ, Paffett MT, Vaniman DT, Heiken G (1991) Lunar surface composition and solar wind-induced secondary ion mass spectrometry. Geophys Res Lett 18:2165–2168

Elphic RC, Delory GT, Hine BP, Mahaffy PR, Horányi M, Colaprete A, Benna M, Noble SK (2014) The lunar atmosphere and dust environment explorer mission. Space Sci Rev 185:3–25

Ennico K, Shirley M, Colaprete A, Osetinsky L (2011) The lunar crater observation and sensing satellite (LCROSS) payload development and performance in flight. Space Sci Rev 167:23–69

Farrell WM, Kaiser ML, Steinberg JT (1997) Electrostatic instability in the central lunar wake: A process for replenishing the plasma void? Geophys Res Lett 24:1135–1138

Farrell WM, Kaiser ML, Steinberg JT, Bale SD (1998) A simple simulation of a plasma void: Applications to wind observations of the lunar wake. J Geophys Res 103:23653–23660

Farrell WM, Tribble AC, Steinberg JT (2002) Similarities between the plasma wake of the Moon and Space Shuttle. J Spacecraft Rockets 39:749

Farrell WM, Stubbs TJ, Halekas JS, Delory GT, Collier MR, Vondrak RR, Lin RP (2008) Loss of solar wind plasma neutrality and affect on surface potentials near the lunar terminator and shadowed polar regions. Geophys Res Lett 35:L05105

Farrell WM, Stubbs TJ, Halekas JS, Killen RM, Delory GT, Collier MR, Vondrak RR (2010) Anticipated electrical environment within permanently shadowed lunar craters. J Geophys Res 115:E03004

Farrell WM, Halekas JS, Killen RM, Delory GT, Gross N, Bleacher LV, Krauss-Varben D, Travnicek P, Hurley D, Stubbs TJ, Zimmerman MI (2012) Solar-Storm/Lunar Atmosphere Model (SSLAM): An overview of the effort and description of the driving storm environment. J Geophys Res 117:E00K04

Farrell WM, Hurley DM, Hodges RR, Killen RM, Halekas JS, Zimmerman MI, Delory GT (2013) Redistribution of lunar polar water to mid-latitudes and its role in forming an OH veneer. Planet Space Sci 89:5–20

Farrell WM, Hurley DM, Zimmerman MI (2015a) Solar wind implantation into lunar regolith: Hydrogen retention in a surface with defects. Icarus 255:116–126

Farrell WM, Hurley DM, Zimmerman MI (2015b) Spillage of lunar polar crater volatiles onto adjacent terrains: The case for dynamic processes. Geophys Res Lett 42:3160–3165

Farrell WM, Hurley DM, Esposito VJ, McLain JL, Zimmerman MI (2017) The statistical mechanics of solar wind hydroxylation at the Moon, within lunar magnetic anomalies, and at Phobos. J Geophys Res Planets 122:269–289

Farrell WM, Hurley DM, Poston MJ, Hayne PO, Szalay JR, McLain JL (2019) The young age of the LAMP-observed frost in lunar polar cold trap. Geophys Res Lett 46:8680–8688

Fatemi S, Holmström M, Futaana Y (2012) The effects of lunar surface plasma absorption and solar wind temperature anisotropies on the solar wind proton velocity space distributions in the low-altitude lunar plasma wake. J Geophys Res 117:A10105

Fatemi S, Holmström M, Futaana Y, Barabash S, Lue C (2013) The lunar wake current systems. Geophys Res Lett 40:17–21

Fatemi S, Holmström M, Futaana Y, Lue C, Collier MR, Barabash S, Stenberg G (2014) Effects of protons reflected by lunar crustal magnetic fields on the global lunar plasma environment. J Geophys Res 119:6095–6105

Fatemi S, Lue C, Holmström M, Poppe AR, Wieser M, Barabash S, Delory GT (2015a) Solar wind plasma interaction with Gerasimovich lunar magnetic anomaly. J Geophys Res 120:4719–4735

Fatemi S, Fuqua HA, Poppe AR, Delory GT, Halekas JS, Farrell WM, Holmström M (2015b) On the confinement of lunar induced magnetic fields. Geophys Res Lett 42:6931–6938

Feldman PD, Hurley DM, Retherford KD, Gladstone GR, Stern SA, Pryor W, Parker JW, Kaufmann DE, Davis MW, Versteeg MH (2012) Temporal variability of lunar exospheric helium during January 2012 from LRO/LAMP. Icarus 221:854–858

Feldman PD, Glenar DA, Stubbs TJ, Retherford KD, Gladstone GR, Miles PF, Greathouse TK, Kaufmann DE, Parker JW, Stern SA (2014) Upper limits for a lunar dust exosphere from far-ultraviolet spectroscopy by LRO/LAMP. Icarus 233:106–113

Fink D, Krauser J, Nagengast D, Murphy TA, Erxmeier J, Palmetshofer L, Bräunig D, Weidinger A (1995) Hydrogen implantation and diffusion in silicon and silicon dioxide. Appl Phys A 61:381–388

Flanagan TM, Goree, J (2006) Dust release from surfaces exposed to plasma. Phys Plasmas 13:123504

Funsten HO, Allegrini F, Bochsler PA, Fuselier SA, Gruntman M, Henderson K, Janzen PH, Johnson RE, Larsen BA, Lawrence DJ, McComas DJ (2013) Reflection of solar wind hydrogen from the lunar surface. J Geophys Res 118:292–305

Futaana Y, Machida S, Saito Y, Matsuoka A, Hayakawa H (2001) Counterstreaming electrons in the near vicinity of the Moon observed by plasma instruments on board NOZOMI. J Geophys Res 106:18729–18740
Futaana Y, Machida S, Saito Y, Matsuoka A, Hayakawa (2003) Moon-related nonthermal ions observed by Nozomi: Species, sources, and generation mechanisms. J Geophys Res 108:1025
Futaana Y, Barabash S, Holmström M, Bhardwaj A (2006) Low energy neutral atoms imaging of the Moon. Planet Space Sci 54:132–143
Futaana Y, Barabash S, Wieser M, Holmström M, Bhardwaj A, Dhanya MB, Sridharan R, Wurz P, Schaufelberger A, Asamura K (2010) Protons in the near-lunar wake observed by the sub-keV atom reflection analyzer on board Chandrayaan-1. J Geophys Res 115:A10248
Futaana Y, Barabash S, Wieser M, Holmström M, Lue C, Wurz P, Schaufelberger A, Bhardwaj A, Dhanya MB, Asamura K (2012) Empirical energy spectra of neutralized solar wind protons from the lunar regolith. J Geophys Res 117:E05005
Futaana Y, Barabash S, Wieser M, Lue C, Wurz P, Vorburger A, Bhardwaj A, Asamura K (2013) Remote energetic neutral atom imaging of electric potential over a lunar magnetic anomaly. Geophys Res Lett 40:262–266
Gaddis LR, Joy KH, Bussey BJ, Carpenter JD, Crawford IA, Elphic RC, Halekas JS, Lawrence SJ, Xiao L (2023) Recent exploration of the Moon: Science from lunar missions since 2006. Rev Mineral Geochem 89:1–51
Garrick-Bethell I, Head III JW, Pieters CM (2011) Spectral properties, magnetic fields, and dust transport at lunar swirls. Icarus 212:480–492
Gladstone GR, Hurley DM, Retherford KD, Feldman PD, Pryor WR, Chaufray JY, Versteeg M, Greathouse TK, Steffl AJ, Throop H, Parker JW (2010) LRO-LAMP observations of the LCROSS impact plume. Science 330:472–476
Glenar DA, Stubbs TJ, McCoy JE, Vondrak RR (2011) A reanalysis of the Apollo light scattering observations, and implications for lunar exospheric dust. Planet Space Sci 59:1695–1707
Glenar DA, Stubbs TJ, Hahn JM, Wang Y (2014) Search for a high-altitude lunar dust exosphere using Clementine navigational star tracker measurements. J Geophys Res Planets 2548–2567
Grard RJL, Tunaley JKE (1971) Photoelectron sheath near a planar probe in interplanetary space. J Geophys Res 76:10
Grava C, Retherford KD, Hurley DM, Feldman PD, Gladstone GR, Greathouse TK, Cook JC, Stern SA, Pryor WR, Halekas JS, Kaufmann DE (2016) Lunar exospheric helium observations of LRO/LAMP coordinated with ARTEMIS. Icarus 273:36–44
Grava C, Stubbs TJ, Glenar DA, Retherford KD, Kaufmann DE (2017) Absence of a detectable lunar nanodust exosphere during a search with LRO's LAMP UV imaging spectrograph. Geophys Res Lett 44:4591–4598
Grün E, Horányi M (2013) A new look at Apollo 17 LEAM data: Nighttime dust activity in 1976. Planet Space Sci 89:2–14
Grün E, Pailer N, Fechtig H, Kissel J (1980) Orbital and physical characteristics of micrometeoroids in the inner solar system as observed by Helios 1. Planet Space Sci 28:333–349
Grün E, Zook HA, Fechtig H, Giese RH (1985) Collisional balance of the meteoritic complex. Icarus 62:244–272
Guernsey RL, Fu JHM (1970) Potential distribution surrounding a photo-emitting plate in a dilute plasma. J Geophys Res 75:16
Gurevich AV, Pitaevskii LP, Smirnova VV (1969) Ionospheric aerodynamics. Space Sci Rev 9:805–871.
Hahn JM, Zook HA, Cooper B, Sunkara B (2002) Clementine observations of the zodiacal light and the dust content of the inner solar system. Icarus 158:360–378
Halekas JS, Lin RP, Mitchell DL (2005a) Large negative lunar surface potentials in sunlight and shadow. Geophys Res Lett 32:L09102
Halekas JS, Bale SD, Mitchell DL, Lin RP (2005b) Magnetic fields and electrons in the lunar plasma wake. J Geophys Res 110:A07222
Halekas JS, Brain DA, Mitchell DL, Lin RP (2006) Whistler waves observed near lunar crustal magnetic sources. Geophys Res Lett 33:L22104
Halekas JS, Delory GT, Brain DA, Lin RP, Fillingim MO, Lee CO, Mewaldt RA, Stubbs TJ, Farrell WM, Hudson MK (2007) Extreme lunar surface charging during solar energetic particle events. Geophys Res Lett 34:L02111
Halekas JS, Brain DA, Lin RP, Mitchell DL (2008a) Solar wind interaction with lunar crustal magnetic anomalies. J Adv Space Res 41:1319–1324
Halekas JS, Delory GT, Lin RP, Stubbs TJ, Farrell WM (2008b) Lunar Prospector observations of the electrostatic potential of the lunar surface and its response to incident currents. J Geophys Res 113:A09102
Halekas JS, Delory GT, Lin RP, Stubbs TJ, Farrell WM (2009a) Lunar Prospector measurements of secondary electron emission from lunar regolith. Planet Space Sci 57:78–82
Halekas JS, Delory GT, Lin RP, Stubbs TJ, Farrell WM (2009b) Lunar surface charging during solar energetic particle events: Measurement and prediction. J Geophys Res 114:A05110
Halekas JS, Saito Y, Delory GT, Farrell WM (2011a) New views of the lunar plasma environment. Planet Space Sci 59:1681–1694
Halekas JS, Angelopoulos V, Sibeck DG, Khurana KK, Russell CT, Delory GT, Farrell WM, McFadden JP, Bonnell JW, Larson D, Ergun RE, Plaschke F, Glassmeier KG (2011b) First results from ARTEMIS, a new two-spacecraft lunar mission: Counter-streaming plasma populations in the lunar wake. *In:* The ARTEMIS Mission. (Russell C, Angelopoulos, V eds) Springer, New York, NY, p 93–107

Halekas JS, Poppe AR, Farrell WM, Delory GT, Angelopoulos V, McFadden JP, Bonnell JW, Glassmeier K-H, Plaschke F, Roux A, Ergun RE (2012a) Lunar precursor effects in the solar wind and terrestrial magnetosphere. J Geophys Res 117:A05101

Halekas JS, Poppe AR, Delory GT, Sarantos M, Farrell WM, Angelopoulos V, McFadden JP (2012b) Lunar pickup ions observed by ARTEMIS: Spatial and temporal distribution and constraints on species and source locations. J Geophys Res 117:E06006

Halekas JS, Poppe AR, Delory GT, Farrell WM, Horányi M (2012c) Solar wind electron interaction with dayside lunar surface and crustal magnetic fields: Evidence for precursor effects. Earth Planets Space 64:73–82

Halekas JS, Poppe AR, Delory GT, Sarantos M, McFadden JP (2013a) Using ARTEMIS pickup ion observations to place constraints on the lunar atmosphere. J Geophys Res Planets 118:81–88

Halekas JS, Poppe AR, McFadden JP, Glassmeier K-H (2013b) The effects of reflected protons on the plasma environment of the moon for parallel interplanetary magnetic fields. Geophys Res Lett 40:4544–4548

Halekas JS, Poppe AR, McFadden JP, Angelopoulos V, Glassmeier K-H, Brain DA (2014a) Evidence for small-scale collisionless shocks at the Moon from ARTEMIS. Geophys Res Lett 41:7436–7443

Halekas JS, Poppe AR, McFadden JP (2014b) The effects of solar wind velocity distributions on the refilling of the lunar wake: ARTEMIS observations and comparisons to one-dimensional theory. J Geophys Res 119:5133–5149

Halekas JS, Benna M, Mahaffy PR, Elphic RC, Poppe AR, Delory CT (2015) Detections of lunar exospheric ions by the LADEE neutral mass spectrometer. Geophys Res Lett 42:5162–5169

Halekas JS, Poppe AR, Farrell WM, McFadden JP (2016) Structure and composition of the distant lunar exosphere: Constraints from ARTEMIS observations of ion acceleration in time-varying fields. J Geophys Res Planets 121:1102–1115

Halekas JS, Poppe AR, Lue C, Farrell WM, McFadden JP (2017) Distribution and solar wind control of compressional solar wind-magnetic anomaly interactions observed at the Moon by ARTEMIS. J Geophys Res Space Phys 122:6240–6254

Harada Y, Machida S, Halekas JS, Poppe AR, McFadden JP (2013) ARTEMIS observations of lunar dayside plasma in the terrestrial magnetotail lobe. J Geophys Res 118:3042–3054

Harada Y, Halekas JS, Poppe AR, Kurita S, McFadden JP (2014) Extended lunar precursor regions: Electron-wave interaction. J Geophys Res 119:9160–9173

Harada Y, Halekas JS, Poppe AR, Tsugawa Y, Kurita S, McFadden JP (2015) Statistical characterization of the foremoon particle and wave morphology: ARTEMIS observations. J Geophys Res 120:4907–4921

Harada Y, Halekas JS (2016) Upstream waves and particles at the Moon. *In*: Low-Frequency Waves in Space Plasmas, Keiling A, Lee D-H, Nakariakov V (eds) Wiley, Hoboken, NJ

Harada Y, Poppe AR, Halekas JS, Chamberlin PC, McFadden JP (2017) Photoemission and electrostatic potentals on the dayside lunar surface in the terrestrial magnetotail lobes. Geophys Res Lett 44:5276–5282

Hartle RE, Killen RM (2006) Measuring pickup ions to characterize the surfaces and exospheres of planetary bodies: Applications to the Moon. Geophys Res Lett 33:L05201

Hartzell CM, Wang X, Scheeres DJ, Horányi M (2013) Experimental demonstration of the role of cohesion in electrostatic dust lofting. Geophys Res Lett 40:1038–1042

Haruyama J, Hioki K, Shirao M, Morota T, Hiesinger H, van der Bogart CH, Miyamoto H, Iwasaki A, Yokota Y, Ohtake M, Matsunaga T, Hara S, Nakanotani S, Pieters CM (2009) Possible lunar lava tube skylight observed by SELENE cameras. Geophys Res Lett 36:L21206

Hashimoto K, Hashitani M, Kasahara Y, Omura Y, Nishino MN, Saito Y, Yokota S, Ono T, Tsunakawa H, Shibuya H, Matsushima M, Shimizu H, Takahashi F (2010) Electrostatic solitary waves associated with magnetic anomalies and wake boundary of the Moon observed by Kayguya. Geophys Res Lett 37:L19204

Hayderer G, Cernusca S, Schmid M, Varga P, Winter HP, Aumayr F, Niemann D, Hoffmann V, Stolterfoht N, Lemell C, Wirtz L, Burgdorfer J (2001) Kinetically assisted potential sputtering of insulators by highly charged ions. Phys Rev Lett 86:3530–3533

Heijmans LCJ, Nijdam S (2016) Dust on a surface in a plasma: A charge simulation. Phys Plasmas 23:043703

Hendrix AR, Retherford KD, Randall Gladstone G, Hurley DM, Feldman PD, Egan AF, Kaufmann DE, Miles PF, Parker JW, Horvath D, Rojas PM (2012) The lunar far-UV albedo: Indicator of hydration and weathering. J Geophys Res 117:E12001

Hendrix AR, Hurley DM, Farrell WM, Greenhagen BT, Hayne PO, Retherford KD, Vilas F, Cahill JT, Poston MJ, Liu Y (2019) Diurnally migrating lunar water: Evidence from ultraviolet data. Geophys Res Lett 46:2417–2424

Hibbitts CA, Grieves GA, Poston MJ, Dyar MD, Alexandrov AB, Johnson MA, Orlando TM (2011) Thermal stability of water and hydroxyl on the surface of the Moon from temperature-programmed desorption measurements of lunar analog materials. Icarus 213:64–72

Hilchenbach M, Hovestadt D, Klecker B, Mobius E (1991) Detection of singly ionized energetic lunar pick-up ions upstream of Earth's bow shock. *In*: Solar Wind Seven. Marsch E, Schwenn G (eds), Pergamon, New York, p 150–155

Hilchenbach M, Hovestadt D, Klecker B, Mobius E (1993) Observation of energetic lunar pick-up ions near Earth. Adv Space Res 13:321–324

Hobbs GD, Wesson JA (1967) Research notes: Heat flow through a Langmuir sheath in the presence of electron emission. Plasma Phys 9:85–87

Hodges RR (1977) Release of radiogenic gases from the moon. Phys Earth Planet Int 14:282–288

Hodges RR (2011) Resolution of the lunar hydrogen enigma. Geophys Res Lett 38:L06201
Hodges RR (2016) Methane in the lunar exosphere: Implications for solar wind carbon escape. Geophys Res Lett 43:6742–6748
Hodges RR (2018) Semiannual Oscillations of the lunar exosphere: Implications for the water and polar ice. Geophys Res Lett 45:7409–7416
Hodges RR, Hoffman JH (1974) Measurements of solar wind helium in the lunar atmosphere. Geophys Res Lett 1:69–71
Hodges RR, Hoffman JH (1975) Implications of atmospheric Ar-40 escape on the interior structure of the moon. Lunar Planet Sci Conf Proc 6:3039–3047
Hodges RR, Johnson RS (1968) Lateral transport in planetary exospheres. J Geophys Res 73:7307–7317
Hodges RR, Mahaffy PR (2016) Synodic and semiannual oscillations of argon-40 in the lunar exosphere. Geophys Res Lett 43:22–27
Hodges RR, Hoffman JH, Johnson FS (1974) The lunar atmosphere. Icarus 21:415–426
Hoffman JH, Hodges RR, Johnson FS, Evans DE (1973) Lunar atmospheric composition results from Apollo 17. Lunar Planet Sci Conf Proc 4:2865
Holmström M, Weiser M, Barabash S, Futaana Y, Bhardwaj A (2010) Dynamics of solar wind protons reflected by the Moon. J Geophys Res 115:A06206
Holmström M, Fatemi S, Futaana Y, Nilsson H (2012) The interaction between the Moon and the solar wind. Earth Planets Space 64:237–245
Hood LL, Zakharian A, Halekas J, Mitchell DL, Lin RP, Acuña MH, Binder AB (2001) Initial mapping and interpretation of lunar crustal magnetic anomalies using Lunar Prospector magnetometer data. J Geophys Res 106:27825–27840
Horányi M, Sternovsky Z, Lankton M, Dumont C, Gagnard S, Gathrigh D, Grün E, Hansen D, James D, Kempf S, Lamprecht B, Srama R, Szalay JR, Wright G (2014) The Lunar Dust Experiment (LDEX) onboard the Lunar Atmosphere and Dust Environment Explorer (LADEE) mission. Space Sci Rev 185:93–113
Horányi M, Szalay J, Kempf S, Schmidt J, Grün E, Srama R, Sternovsky Z (2015) A permanent, asymmetric dust cloud around the Moon. Nature 522: 324–326
Howes CT, Wang X, Deca J, Horányi M (2015) Laboratory investigation of lunar surface electric potentials in magnetic anomaly regions. Geophys Res Lett 42:4280–4287
Hurley DM, Benna M (2017) Simulations of lunar exospheric water events from micro-meteoroid impact. Planet Space Sci 162:148–156
Hurley DM, Lawrence DJ, Bussey DBJ, Vondrak RR, Elphic RC, Gladstone GR (2012) Two-dimensional distribution of volatiles in the lunar regolith from space weathering simulations. Geophys Res Lett 39:L09203
Hurley DM, Cook JC, Benna M, Halekas JS, Feldman PD, Retherford KD, Greathouse T (2016) Understanding temporal and spatial variability of the lunar helium atmosphere using simultaneous observations from LRO, LADEE, and ARTEMIS. Icarus 273:45–52
Hurley DM, Cook JC, Retherford KD, Greathouse T, Gladstone GR, Mandt K, Pryor W (2017) Contributions of solar wind and micrometeoroids to molecular hydrogen in the lunar exosphere. Icarus 283:31–37
Hutchinson IH (2012) Electron velocity distribution instability in magnetized plasma wakes and artificial electron mass. J Geophys Res 117:A03101
Iglseder H, Uesugi K, Svedhem H (1996) Cosmic dust measurements in lunar orbit. Adv Space Res 17:177–182
Jackson TL, Farrell WM, Killen RM, Delory GT, Halekas JS, Stubbs TJ (2011) Discharging of roving objects in the lunar polar regions. J Spacecraft Rockets 48:700–703
Jackson, TL, Farrell WM, Zimmerman MI (2015) Rover wheel charging on the lunar surface. Adv Space Sci 55:1710–1720
Janches D, Mathews JD, Meisel DD, Getman VS, Zhou QH (2000) Doppler studies of near-antapex UHF radar micrometeors. Icarus 143:347–353
Jarvinen R, Alho M, Kallio E, Wurz P, Barabash S, Futaana Y (2014) On vertical electric fields at lunar magnetic anomalies. Geophys Res Lett 41:2243–2249
Jolliff BL, Gillis JJ, Haskin LA, Korotev RL, Wieczorek MA (2000) Major lunar crustal terranes: Surface expressions and crust-mantle origins. J Geophys Res Planets 105(E2):4197–4216
Jolliff BL, Wieczorek MA, Shearer CK, Neal CR (Eds) (2006) New Views of the Moon. Reviews in Mineralogy and Geochemistry, vol. 60. Mineralogical Society of America
Jones J, Brown P (1993) Sporadic meteor radiant distributions—Orbital survey results. MNRAS 265:524–532
Jones BM, Aleksandrov A, Hibbitts K, Dyar MD, Orlando TM (2018) Solar wind-induced water cycle on the Moon. Geophys Res Lett 45:10959–10967
Kagitani M, Taguchi M, Yamazaki A, Yoshikawa I, Murakami G, Yoshioka K, Okano S (2010) Variation in lunar sodium exosphere measured from lunar orbiter SELENE (Kaguya). Planet Space Sci 58:1660–1664
Killen RM, Morgan TH (1993) Maintaining the Na atmosphere of Mercury. Icarus 101:293–312
Killen RM, Potter AE, Hurley DM, Plymate C, Naidu S (2010) Observations of the lunar impact plume from the LCROSS event. Geophys Res Lett 37:L23201
Killen RM, Hurley DM, Farrell WM (2012) The effect on the lunar exosphere of a coronal mass ejection. J Geophys Res 117:E00K02

Killen RM, Burger MH, Farrell WM (2017) Exospheric escape: A parametrical study. Adv Space Res 62:2364–2371
Killen RM, Williams DR, Park J, Tucker OJ, Kim SJ (2019) The lunar neon exosphere seen in LACE data. Icarus 329:246–250
Klima R, Cahill J, Hagerty J, Lawrence D (2013) Remote detection of magmatic water in Bulliadus crater on the Moon. Nat Geosci 6:737–741
Kracher A, Aumayr F, Sears DWG, Kareev M (2003) Space weathering by highly charged heavy ions in the solar wind. 66th Annu Met Soc Meeting Abstract 5204
Kramer GY, Besse S, Dhingra D, Nettles J, Klima R, Garrick-Bethell I, Clark RN, Combe JP, Head JW, Taylor LA, Pieters CM, Boardman J, McCord TB (2011) M3 spectral analysis of lunar swirls and the link between optical maturation and surface hydroxyl formation at magnetic anomalies. J Geophys Res 116:E00G18
Krivov AV, Sremčević M, Spahn F, Dikarev VV, Kholshevnikov KV (2003) Impact-generated dust clouds around planetary satellites: spherically symmetric case. Planet Space Sci 51:251–269
Kruger H, Krivov AV, Sremčević M, Grün E (2003) Impact-generated dust clouds surrounding the Galilean moons. Icarus 164:170–187
Kurucz RL, Furenlid I, Brault J, Testerman L (1984) Solar Flux Atlas from 296 to 1300 nm. National Solar Observatory Atlas No. 1
Lin RP, Mitchell DL, Curtis DW, Anderson KA, Carlson CW, McFadden J, Acuña MH, Hood LL, Binder A (1998) Lunar surface magnetic fields and their interaction with the solar wind: Results from Lunar Prospector. Science 281:1480–1484
Love SG, Brownlee DE (1993) A direct measurement of the terrestrial mass accretion rate of cosmic dust. Science 262:550–553
Lue C, Futaana Y, Barabash S, Wieser M, Holmström M, Bhardwaj A, Dhanya MB, Wurz P (2011) Strong influence of lunar crustal fields on the solar wind flow. Geophys Res Lett 38:L03202
Lue C, Futaana Y, Barabash S, Wieser M, Bhardwaj A, Wurz P (2014) Chandrayaan-1 observations of backscattered solar wind protons from the lunar regolith: Dependence on the solar wind speed. J Geophys Res 119:968–975
Lue C, Halekas JS, Poppe AR, McFadden JP (2018) ARTEMIS observations of solar wind proton scattering off the lunar surface. J Geophys Res 123:5289–5299
Luo QY, Yang L, Ji JH (2016) Global distribution of the kinetic scale magnetic turbulence around the Moon. Astrophys J Lett 816:L3
Madey TE, Yakshinskiy BV, Ageev VN, Johnson RE (1998) Desorption of alkali atoms and ions from oxide surfaces: Relative to the origins of Na and K in atmospheres of Mercury and the Moon. J Geophys Res 103:5873–5877
Madey TE, Johnson RE, Orlando TM (2002) Far-out surface science: radiation-induced surface processes in the solar system. Surf Sci 500:838–858
Mall U, Kirsch E, Cierpka K, Wilken B, Söding A, Neubauer F, Gloeckler G, Galvin A (1998) Direct observation of lunar pick-up ions near the Moon. Geophys Res Lett 25:3799–3802
Marchi S, Morbidelli A, Cremonese G (2005) Flux of meteoroid impacts on Mercury. Astron Astrophys 431:1123–1127
McComas DJ, Allegrini F, Bochsler P, Frisch P, Funsten HO, Gruntman M, Schwadron NA (2009) Lunar backscatter and neutralization of the solar wind: First observations of neutral atoms from the Moon. Geophys Res Lett 36: L12104
McCord TB, Taylor LA, Combe JP, Kramer G, Pieters CM, Sunshine JM, Clark RN (2011) Sources and physical processes responsible for OH/H_2O in the lunar soil as revealed by the Moon Mineralogy Mapper (M3). J Geophys Res 116:E00G05
McCord TB, Li JY, Combe JP, McSween HY, Jaumann R, Reddy V, Tosi F, Williams DA, Blewett DT, Turrini D, Palomba E, Pieters CM, De Sanctis MC, Ammannito E, Capria MT, Le Corre L, Longobardo A, Nathues A, Mittlefehldt DW, Schröder SE, Hiesinger H, Beck AW, Capaccioni F, Carsenty U, Keller HU, Denevi BW, Sunshine JM, Raymond CA, Russell CT (2012) Dark material on Vesta from the infall of carbonaceous volatile-rich material. Nature 491:83
McCoy JE (1976) Photometric studies of light scattering above the lunar terminator from Apollo solar corona photography. Lunar Planet Sci Conf Proc 7:1087–1112
McCoy JE, Criswell DR (1974) Evidence for a high latitude distribution of lunar dust. The 5th Proc Lunar Sci Conf :2991
McDonnell T, McBride N, Green SF, Ratcliff PR, Gardner DJ, Griffiths AD (2001) Near earth environment. *In:* Interplanetary Dust, Grün E, Gustafson BAS, Dermott SF, Fechtig H (Eds) Springer, New York, p 165–231
McGrath MA, Johnson RE, Lanzerotti LJ (1986) Sputtering of sodium on the planet Mercury. Nature 323:694–696
Mendillo M, Baumgardner J (1995) Constraints on the origin of the Moon's atmosphere from observations during a lunar eclipse. Nature 377:404
Mendillo M, Baumgardner J, Wilson J (1999) Observational test for the solar wind sputtering origin of the Moon's extended sodium atmosphere. Icarus 137:13–23
Merkel AW, Vervack Jr RJ, Killen RM, Cassidy TA, McClintock WE, Nittler LR, Burger MH (2018) Evidence connecting Mercury's magnesium exosphere to its magnesium-rich surface terrane. Geophys Res Lett 45:6790–6797
Mihalov JD, Sonett CP, Binsack JH, Moutsoulas MD (1971) Possible fossil lunar magnetism inferred from satellite data. Science 171:892– 95
Milliken RE, Li S (2017) Remote detection of widespread indigenous water in lunar pyroclastic deposits. Nat Geosci 10:561–565

Mitchell CJ, Horányi M, Havnes O, Porco CC (2006) Saturn's spokes: Lost and found. Science 311:1587–1589
Miyake Y, Nishino MN (2015) Electrostatic environment near lunar vertical hole: 3D plasma particle simulations. Icarus 260:301–307
Morgan TH, Shemansky DE (1991) Limits to the lunar atmosphere. J Geophys Res 96:1351–1367
Nakagawa T, Takahashi Y, Iizima M (2003) GEOTAIL observation of upstream ULF waves associated with the lunar wake. Earth Planets Space 55:569–580
Nakagawa T, Takahashi F, Tsunakawa H, Shibuya H, Shimizu H, Matsushima M (2011) Non-monochromatic whistler waves detected by Kaguya on the dayside surface of the moon. Earth Planets Space 63:37–46
Nakagawa T, Nakayama A, Takahashi F, Tsunakawa H, Shibuya H, Shimizu H, Matsushima M (2012) Large-amplitude monochromatic ULF waves detected by Kaguya at the Moon. J Geophys Res 117:A04101
Nakagawa T, Nakashima T, Wada T, Tsunakawa H, Takahashi F, Shibuya H, Shimizu H, Matsushima M, Saito Y (2015) ELF magnetic fluctuations detected by Kaguya in deepest lunar wake associated with type-II protons. Earth Planets Space 67:50
Nakagawa T, Nishino MN, Tsunakawa H, Takahashi F, Shibuya H, Shimizu H, Saito Y (2018) Electromagnetic ion cyclotron waves detected by Kaguya and Geotail in the Earth's magnetotail. J Geophys Res 123:1146–1164
Nakamura Y (1977) HFT events: Shallow moonquakes? Phys Earth Planet Int 14: 217–223
Neckel H, Labs D (1981) Improved data of solar spectral irradiance from 0.33 to 1.25 microns. Solar Phys 74:231–249
Ness NF, Behannon KW, Taylor HE, Whang YC (1968) Perturbations of the interplanetary magnetic field by the lunar wake. J Geophys Res 73:3421–3440
Nishino MN, Maezawa K, Fujimoto M, Saito Y, Yokota Y, Asamura K, Tanaka T, Tsunakawa H, Matsushima M, Takahashi F, Terasawa T, Shibuya H, Shimizu H (2009a) Pairwise energy gain-loss feature of solar wind protons in the near-Moon wake. Geophys Res Lett 36:L12108
Nishino MN, Fujimoto M, Maezawa K, Saito Y, Yokota S, Asamura K, Tanaka T, Tsunakawa H, Matsushima M, Takahashi F, Terasawa T, Shibuya H, Shimizu H (2009b) Solar-wind proton access deep into the near-Moon wake. Geophys Res Lett 36:L16103
Nishino MN, Fujimoto M, Saito Y, Yokota S, Kasahara Y, Omura Y, Goto Y, Hashimoto K, Kumamoto A, Ono T, Tsunakawa H, Matsushima M, Takahashi F, Shibuya H, Shimizu H, Terasawa T (2010) Effect of the solar wind proton entry into the deepest lunar wake. Geophys Res Lett 37:L12106
Nishino MN, Wang XD, Fujimoto M, Tsunakawa H, Saito Y, Yokota S, Bian W, Matsushima M, Shibuya H, Shimiziu H, Takahashi F, Terasawa T (2011) Anomalous deformation of the Earth's bow shock in the lunar wake: Joint measurement by Chang'E-1 and SELENE. Planet Space Sci 59:378–386
Nishino MN, Harada Y, Saito Y, Tsunakawa H, Takahashi F, Yokota S, Matsushima M, Shibuya H, Shimizu H (2017) Kaguya observations of the lunar wake in the terrestrial foreshock: Surface potential change by bow-shock reflected ions. Icarus 293:45–51
Nitter T, Havnes O, Melands F (1998) Levitation and dynamics of charged dust in the photoelectron sheath above surfaces in space. J Geophys Res 103:6605–6620
O'Brien BJ (2011) Review of measurement of dust movements on the Moon during Apollo. Planet Space Sci 59:1708–1726
Ogilvie KW Ness NF (1969) Dependence of the lunar wake on solar wind plasma characteristics. J Geophys Res 74:4123
Ogilvie KW, Steinberg JT, Fitzenreiter RJ, Owen CJ, Lazarus AJ, Farrell WM, Torbert RB (1996) Observations of the lunar plasma wake from the WIND spacecraft on December 27, 1994. Geophys Res Lett 10:1255–1258
Owen CJ, Lepping RP, Ogilvie KW, Slavin JA, Farrell WM, Byrnes JB (1996) The lunar wake at 6.8 RL: WIND magnetic field observations. Geophys Res Lett 10:1263–1266
Paige DA, Siegler MA, Zhang JA, Hayne PO, Greenhagen BT, Foote MC, Siegler MA, Vasavada AR, Paige DA (2010) Diviner lunar radiometer observations of cold traps in the Moon's south polar region. Science 330:479–482
Pieters CM, Goswami JN, Clark RN, Annadurai M, Boardman J, Buratti B, Combe JP, Dyar MD, Green R, Head JW, Hibbitts C (2009) Character and spatial distribution of OH/H_2O on the surface of the Moon seen by M3 on Chandrayaan-1. Science 325:568–572
Piquette M, Horányi M (2017) The effect of asymmetric surface topography on dust dynamics on airless bodies. Icarus 291: 65–74
Plane JMC (2012) Cosmic dust in the Earth's atmosphere. Chem Soc Rev 41:6507–12
Pokorný P, Vokrouhlický D, Nesvorny D, Campbell-Brown M, Brown P (2014) Dynamical model for the Toroidal Sporadic Meteors. Astrophys J 789:25
Pokorný P, Janches D, Sarantos M, Szalay JR, Horányi M, Nesvorný D, Kuchner MJ (2019) Meteoroids at the Moon: Orbital properties, surface vaporization, and impact ejecta production. J Geophys Res 124:752–778
Poppe AR, Horányi M (2010) Simulations of the photoelectron sheath and dust levitation on the lunar surface. J Geophys Res 115:A08106
Poppe A, Halekas JS, Horányi M (2011) Negative potentials above the day-side lunar surface in the terrestrial plasma sheet: Evidence of nonmonotonic potentials. Geophys Res Lett 38:L02103
Poppe AR, Halekas JS, Delory GT, Farrell WM (2012a) Particle-in-cell simulations of the solar wind interaction with lunar crustal magnetic anomalies: Magnetic cusp regions. J Geophys Res 117:A09105

Poppe AR, Halekas JS, Delory GT, Farrell WM, Angelopoulos V, McFadden JP, Bonnell JW, Ergun RE (2012b) A comparison of ARTEMIS observations and particle-in-cell modeling of the lunar photoelectron sheath in the terrestrial magnetotail. Geophys Res Lett 39:L01102

Poppe AR, Samad R, Halekas JS, Sarantos M, Delory GT, Farrell WM, Angelopoulos V, McFadden JP (2012c) ARTEMIS observations of lunar pickup ions in the terrestrial magnetotail lobes. Geophys Res Lett 39:L17104

Poppe AR, Piquette M, Likhanskii A, Horányi M (2012d) The effect of surface topography on the lunar photoelectron sheath and electrostatic dust transport. Icarus 221:135–146

Poppe AR, Sarantos M, Halekas JS, Delory GT, Saito Y, Nishino M (2014a) Anisotropic solar wind sputtering of the lunar surface induced by crustal magnetic anomalies. Geophys Res Lett 41:4865–4872

Poppe AR, Fatemi S, Halekas JS, Holmström M, Delory GT (2014b) ARTEMIS observations of extreme diamagnetic fields in the lunar wake. Geophys Res Lett 41:3766–3773

Poppe AR, Halekas JS, Szalay JR, Horányi M, Levin Z, Kempf S (2016a) LADEE/LDEX observations of lunar pick-up ion variability. Geophys Res Lett 43:3069–3077

Poppe AR, Fillingim MO, Halekas JS, Raeder J, Angelopoulos V (2016b) ARTEMIS observations of terrestrial ionospheric molecular ion outflow at the Moon. Geophys Res Lett 43:6749–6758

Poppe AR, Halekas JS, Lue C, Fatemi S (2017) ARTEMIS observations of the solar wind proton scattering function from lunar crustal magnetic anomalies. J Geophys Res 122:771–783

Poston MJ, Grieves GA, Aleksandrov AB, Hibbitts CA, Darby Dyar M, Orlando TM (2013) Water interactions with micronized lunar surrogates JSC-1A and albite under ultra-high vacuum with application to lunar observations. J Geophys Res 118:105–115

Poston MJ, Grieves GA, Aleksandrov AB, Hibbitts CA, Dyar MD, Orlando TM (2015) Temperature programmed desorption studies of water interactions with Apollo lunar samples 12001 and 72501. Icarus 255:24–29

Potter AE, Morgan TH (1988) Discovery of sodium and potassium vapor in the atmosphere of the Moon. Science 241:675–680

Potter AE, Morgan TH (1994) Variation of lunar sodium emission intensity with phase angle. Geophys Res Lett 21:2263–2266

Potter AE, Killen RM, Morgan TH (2000) Variation of lunar sodium during passage of the Moon through the Earth's magnetotail. J Geophys Res 105(E6):15073–15084

Rennilson JJ, Criswell DR (1974) Surveyor observations of lunar horizon-glow. Moon 10:121–142

Robinson MS, Thomas PC, Veverka J, Murchie S, Carcich B (2001) The nature of ponded deposits on Eros. Nature 413:396–400

Robinson MS, Ashley JW, Boyd AK, Wagner RV, Speyerer EJ, Hawke BR, Hiesinger H, Van Der Bogert CH (2012) Confirmation of sublunarean voids and thin layering in mare deposits. Planet Space Sci 69:18–27

Rosborough SA, Oliversen RJ, Mierkiewicz EJ, Sarantos M, Robertson SD, Kuruppuaratchi DC, Derr NJ, Gallant MA, Roesler FL (2019) High-resolution potassium observations of the lunar exosphere. Geophys Res Lett 46:6964–6971

Runcorn SK (1974) On the origin of mascons and moonquakes. Lunar Planet Sci Conf Proc 5:3115–3126

Russell CT, Lichtenstein BR (1975) On the source of lunar limb compressions. J Geophys Res 80:4700–4711

Saito Y, Yokota S, Tanaka T, Asamura K, Nishino MN, Fujimoto M, Tsunakawa H, Shibuya H, Matsushima M, Shimizu H, Takahashi F (2008) Solar wind proton reflection at the lunar surface: Low energy ion measurements by MAP-PACE onboard SELENE (Kayguya). Geophys Res Lett 35:L24205

Saito Y, Yokota S, Asamura K, Tanaka T, Nishino MN, Yamamoto T, Terakawa Y, Fujimoto M, Hasegawa H, Hayakawa H, Hirahara M (2010) Inflight performance and initial results of Plasma energy Angle and Composition Experiment (PACE) on SELENE (Kaguya). Space Sci Rev 154:265–303

Saito Y, Nishino MN, Fujimoto M, Yamamoto T, Yokota S, Tsunakawa H, Shibuya H, Matsushima M, Shimizu H, Takahashi F (2012) Simultaneous observation of the electron acceleration and ion deceleration over lunar magnetic anomalies. Earth Planets Space 64:83–92

Samir U, Wright Jr KH, Stone NH (1983) The expansion of a plasma into a vacuum: Basic phenomena and processes and applications to space plasma physics. Rev Geophys 21:1631–1646

Sarantos M, Killen RM, Sharma AS, Slavin JA (2010) Sources of sodium in the lunar exosphere: Modeling using ground-based observations of sodium emission and spacecraft data of the plasma. Icarus 205:364–374

Sarantos M, Killen RM, Glenar DA, Benna M, Stubbs TJ (2012) Metallic species, oxygen and silicon in the lunar exosphere: Upper limits and prospects for LADEE measurements. J Geophys Res 117:A03103

Schultz PH, Hermalyn B, Colaprete A, Ennico K, Shirley M, Marshall WS (2010) The LCROSS cratering experiment. Science 330:468–472

Schwan J, Wang X, Hsu H-W, Grün E, Horányi M (2017) The charge state of electrostatically transported dust on regolith surfaces. Geophys Res Lett 44:3059–3065

Sheridan TE, Hayes A (2011) Charge fluctuations for particles on a surface exposed to plasma. Appl Phys Lett 98:091501

Sheridan TE, Goree J, Chiu YT, Rairden RL, Kiessling JA (1992) Observation of dust shedding from material bodies in a plasma. J Geophys Res 97:2935–2942

Sickafoose AA, Colwell JE, Horányi M, Robertson S (2002) Experimental levitation of dust grains in a plasma sheath. J Geophys Res 107(A11):1408
Siegler MA, Miller RS, Keane JT, Laneuville M, Paige DA, Matsuyama I, Lawrence DJ, Crotts A, Poston MJ (2016) Lunar true polar wander inferred from polar hydrogen. Nature 531:480–501
Simon PC (1981) Solar irradiance between 120 and 400 nm and its variations. ESA and European Physical Society, ESLAB Symposium on Physics of Solar Variations, 14th, Scheveningen, Netherlands, Sept. 16–19, 1980. Solar Physics, vol. 74, Nov. 1981, p. 273–291
Siscoe GL, Lyon EF, Binsach JH, Bridge HS (1969) Experimental evidence for a detached lunar compression wave. J Geophys Res 74:59–69
Smith BA, Soderblom L, Beebe R, Boyce J, Briggs G, Bunker A, Collins SA, Hansen CJ, Johnson TV, Mitchell JL, Terrile RJ (1981) Encounter with Saturn—Voyager-1 imaging science results. Science 212:163–191
Smith BA, Soderblom L, Batson R, Bridges P, Inge JA, Masursky H, Shoemaker E, Beebe R, Boyce J, Briggs G, Bunker A (1982) A new look at the Saturn system—the Voyager-2 images. Science 215:504–537
Smith SM, Wilson JK, Baumgardner J, Mendillo M (1999) Discovery of the distant lunar sodium tail and its enhancement following the Leonid Meteor Shower of 1998. Geophys Res Lett 26:1649–1652
Sonett CP, Mihalov JD (1972) Lunar fossil magnetism and perturbations of the solar wind. J Geophys Res 77:588–60
Spahn F, Albers N, Hörning M, Kempf S (2006) E ring dust sources: Implications from Cassini's dust measurements. Planet Space Sci 54:1024–1032
Sprague AL, Kozlowski R, Hunten DM, Wells WK (1992) The sodium and potassium atmosphere of the Moon and its interaction with the surface. Icarus 96:27–42
Starukhina LV (2006) Polar regions of the moon as a potential repository of solar-wind-implanted gases. Adv Space Res 37:50–58
Stern SA (1999) The lunar atmosphere: History, status, current problems, and context. Rev Geophys 37:453–491
Stern SA, Retherford KD, Tsang CC, Feldman PD, Pryor W, Gladstone GR (2012) Lunar atmospheric helium detections by the LAMP UV spectrograph on the Lunar Reconnaissance Orbiter. Geophys Res Lett 39:L12202
Stern SA, Cook JC, Chaufray J-Y, Feldman PD, Gladstone GR, Retherford KD (2013) Lunar atmospheric H_2 detections by the LAMP UV spectrograph on the Lunar Reconnaissance Orbiter. Icarus 226:1210–1213
Sternovsky Z, Chamberlin P, Horányi M, Robertson S, Wang X (2008) Variability of the lunar photoelectron sheath and dust mobility due to solar activity. J Geophys Res Space Phys 113:A10104
Stubbs TJ, Vondrak RR, Farrell WM (2006) A dynamic fountain model for lunar dust. Adv Space Res 37:59–66
Stubbs TJ, Farrell WM, Halekas JS, Burchill JK, Collier MR, Zimmerman MI, Vondrak RR, Delory GT, Pfaff RE (2014) Dependence of lunar surface charging on solar wind plasma conditions and solar irradiation. Planet Space Sci 90:10–27
Sunshine JM, Farnham TL, Feaga LM, Groussin O, Merlin F, Milliken RE, A'Hearn MF (2009) Temporal and spatial variability of lunar hydration as observed by the Deep Impact spacecraft. Science 326:565–568
Szalay JR, Horányi M (2015a) Annual variation and synodic modulation of the sporadic meteoroid flux to the Moon. Geophys Res Lett 42:10580–10582
Szalay JR, Horányi M (2015b) The search for electrostatically lofted grains above the Moon with the Lunar Dust Experiment. Geophys Res Lett 42:5141–5146
Szalay JR, Horányi M, Colaprete A, Sarantos M (2016) Meteoritic influence on sodium and potassium abundance in the lunar exosphere measured by LADEE. Geophys Res Lett 43:6096–6102
Szalay JR, Horányi M (2016a) Lunar meteoritic gardening rate derived from in situ LADEE/LDEX measurements. Geophys Res Lett 43:4893–4898
Szalay JR, Horányi M (2016b) Detecting meteoroid streams with an in-situ dust detector above an airless body. Icarus 275:221–231
Szalay JR, Horányi M (2016c) The impact ejecta environment of near-earth asteroids. Astrophys J 830:L29
Szalay JR, Pokorný P, Sternovsky Z, Kupihar Z, Poppe AR, Horányi M (2019) Impact ejecta and gardening in the lunar polar regions. J Geophys Res Planets 124:143–154
Tanaka T, Saito Y, Yokota, Asamura K, Nishino MN, Tsunakawa H, Shibuya H, Matsushima M, Shimizu H, Takahashi F, Fujimoto M, Mukai T, Terasawa T (2009) First in situ observation of the Moon-originating ions in the Earth's Magnetosphere by MAP-PACE on SELENE (Kayguya). Geophys Res Lett 22:L22106
Tao JB, Ergun RE, Newman DL, Halekas JS, Andersson L, Angelopoulos V, Bonnell JW, McFadden JP, Cully CM, Auster H-U, Glassmeier K-H, Larson DE, Baumjohann W, Goldman MV (2012) Kinetic instabilities in the lunar wake: ARTEMIS observations. J Geophys Res 117:A03106
Tenishev V, Rubin M, Tucker OJ, Combi MR, Sarantos M (2013) Kinetic modeling of sodium in the lunar exosphere. Icarus 226:1538–1549
Terada K, Yokota S, Saito Y, Kitamura N, Asamura K, Nishino MN (2017) Biogenic oxygen from Earth transported to the Moon by a wind of magnetospheric ions. Nat Astron 1:0026
Thomas N, Davidsson B, El-Maarry MR, Fornasier S, Giacomini L, Gracia-Berná AG, Hviid SF, Ip WH, Jorda L, Keller HU, Knollenberg J (2015) Redistribution of particles across the nucleus of comet 67P/Churyumov-Gerasimenko. Astron Astrophys 583:A17

Thuillier G, Herse M, Simon PC, Labs D, Mandel H, Gillotay D, Foujols T (1998) The Visible Solar spectral irradiance from 350 to 850 nm as measured by the solspec spectrometer during the Atlas I Mission. Solar Phys 177:41–61

Tsugawa Y, Terada N, Katoh Y, Ono T, Tsunakawa F, Takahashi F, Shibuya H, Shimizu H, Matsushima M (2011) Statistical analysis of monochromatic whistler waves near the Moon detected by Kaguya. Ann Geophys 29: 889–893

Tsugawa Y, Katoh Y, Terada N, Ono T, Tsunakawa H, Takahashi F, Shibuya H, Shimizu H, Matsushima M, Saito Y, Yokota S, Nishino MN (2012) Statistical study of broadband whistler-mode waves detected by Kaguya near the Moon. Geophys Res Lett 39:L16101

Tsugawa Y, Katoh Y, Terada N, Ono T, Tsunakawa H, Takahashi F, Shibuya H, Shimizu H, Matsushima M (2014) Group-standing of whistler mode waves near the Moon. J Geophys Res Space Phys 119:2634–2648

Tsugawa Y, Katoh Y, Terada N, Tsunakawa H, Takahashi F, Shibuya H, Shimizu H, Matsushima M (2015) Harmonics of whistler-mode waves near the Moon. Earth Planets Space 67:36

Tsunakawa H, Takahashi F, Shimizu H, Shibuya H, Matsushima M (2015) Surface vector mapping of magnetic anomalies over the Moon using Kaguya and Lunar Prospector observations. J Geophys Res Planets 120:1160–1185

Tucker OJ, Farrell WM, Killen RM, Hurley DM (2019) Solar wind implantation into the lunar regolith: Monte Carlo simulations of H retention in a surface with defects and the H_2 exosphere. J Geophys Res Planets 124:278–293

Tyler AL, Kozlowski RW, Hunten DM (1988) Observations of sodium in the tenuous lunar atmosphere. Geophys Res Lett 15:1141–1144

Verani S, Barbieri C, Benn C, Cremonese G (1998) Possible detection of meteor stream effects on the lunar sodium atmosphere. Planet Space Sci 46:1003–1006

Vernisse Y, Kriegel H, Wiehle S, Motschmann U, Glassmeier KH (2013) Stellar winds and planetary bodies simulations: Lunar type interaction in super-Alfvénic and sub-Alfvénic flows. Planet Space Sci 84:37–44

von Steiger R, Schwadron NA, Fisk LA, Geiss J, Gloeckler G, Hefti S, Wilken B, Wimmer-Schweingruber RF, Zurbuchen TH (2000) Composition of quasi-stationary solar wind flows from Ulysses/Solar Wind Ion Composition Spectrometer. J Geophys Res 105(A12):27,217–27,238

Vorburger A, Wurz P, Barabash S, Wieser M, Futaana Y, Lue C, Holmström M, Bhardwaj A, Dhanya MB, Asamura K (2013) Energetic neutral atom imaging of the lunar surface. J Geophys Res Space Phys 118:3937–3945

Vorburger A, Wurz P, Barabash S, Wieser M, Futaana Y, Holmström M, Bhardwaj A, Asamura K (2014) First direct observation of sputtered lunar oxygen. J Geophys Res 119:709–722

Wang X, Colwell JE, Horányi M, Robertson S (2007) Charge of dust on surfaces in plasma. IEEE Trans Plasma Sci 35:271–279

Wang X, Horányi M, Robertson S (2009) Experiments on dust transport in plasma to investigate the origin of the lunar horizon glow. J Geophys Res 114:A05103

Wang XD, Bian W, Wang JS, Liu JJ, Zou YL, Zhang HB, Lu C, Liu JZ, Zuo W, Su Y, Wen WB, Wang M, Ouyang ZY, Li CL (2010a) Acceleration of scattered solar wind protons at the polar terminator of the Moon: Results from Chang'E-1/SWIDS. Geophys Res Lett 37:L07203

Wang X, Horányi M, Robertson S (2010b) Investigation of dust transport on the lunar surface in a laboratory plasma with an electron beam. J Geophys Res 115:A11102

Wang XD, Zong QG, Wang JS, Cui J, Rème H, Dandouras I, Aoustin C, Tan X, Shen J, Ren X, Liu JJ (2011a) Detection of $m/q = 2$ pickup ions in the plasma environment of the Moon: The trace of exospheric H_2^+. Geophys Res Lett 38:L14204

Wang X, Horányi M, Robertson S (2011b) Dust transport near electron beam impact and shadow boundaries. Planet Space Sci 59:1791–1794

Wang X, Horányi M, Robertson S (2012) Characteristics of a plasma sheath in a magnetic dipole field: Implications to the solar wind interaction with the lunar magnetic anomalies. J Geophys Res 117:A06226

Wang X, Howes CT, Horányi M, Robertson S (2013) Electric potentials in magnetic dipole fields normal and oblique to a surface in plasma: Understanding the solar wind interaction with lunar magnetic anomalies. Geophys Res Lett 40:1686–1690

Wang X, Schwan J, Hsu H-W, Grün E, Horányi M (2016a) Dust charging and transport on airless planetary bodies. Geophys Res Lett 43:6103–6110

Wang X, Pilewskie J, Hsu, H-W, Horányi M (2016b) Plasma potential in the sheaths of electron-emitting surfaces in space. Geophys Res Lett 43:525–531

Whang YC, Ness NF (1970) Observations and interpretation of the lunar Mach cone. J Geophys Res 75:6002–6010

Wieser M, Barabash S, Futaana Y, Holmström M, Bhardwaj A, Sridharan R, Dhanya MB, Wurz P, Schaufelberger A, Asamura K (2009) Extremely high reflection of solar wind protons as neutral hydrogen atoms from regolith in space. Planet Space Sci 57:2132–2134

Wieser M, Barabash S, Futaana Y, Holmström M, Bhardwaj A, Sridharan R, Dhanya MB, Schaufelberger A, Wurz P, Asamura K (2010) First observation of a mini magnetosphere above a lunar magnetic anomaly using energetic neutral atoms. Geophys Res Lett 37:L05103

Wiehle S, Plaschke F, Motschmann U, Glassmeier K-H, Auster HU, Angelopoulos V, Mueller J, Kriegel H, Georgescu E, Halekas J, Sibeck DG, McFadden JP (2011) First lunar wake passage of ARTEMIS: Discrimination of wake effects and solar wind fluctuations by 3D hybrid simulations. Planet Space Sci 59:661–671

Wooden DH, Cook AM, Colaprete A, Glenar DA, Stubbs TJ, Shirley M (2016) Evidence for a dynamic nanodust cloud enveloping the Moon. Nat Geosci 9:665–668
Xu S, Poppe AR, Halekas JS, Mitchell DL, McFadden JP, Harada Y (2019) Mapping the lunar wake potential structures with ARTEMIS data. J Geophys Res Space Phys 124:3360–3377
Yakshinskiy BV, Madey TE (1999) Photon-stimulated desorption as a substantial source of sodium in the lunar atmosphere. Nature 400:642–644
Yakshinskiy BV, Madey TE (2004) Photon-stimulated desorption of Na from a lunar sample: temperature-dependent effects. Icarus 168:53–59
Yokota S, Saito Y, Asamura K, Tanaka T, Nishino MN, Tsunakawa H, Shibuya H, Matsushima M, Shimizu H, Takahashi F, Fujimoto M, Mukai T, Terasawa T (2009) First direct detection of ions originating from the Moon by MAP-PACE IMA onboard SELENE (Kayguya). Geophys Res Lett 36:L11201
Yokota S, Tanaka T, Saito Y, Asamura K, Nishino MN, Fujimoto M, Tsunakawa H, Shibuya H, Matsushima M, Shimizu H, Takahashi F (2014) Structure of the ionized lunar sodium and potassium exosphere: Dawn-dusk asymmetry. J Geophys Res 119:798–809
Zeller EJ, Ronca LB, Levy PW (1966) Proton-induced hydroxyl formation on the lunar surface. J Geophys Res 71:4855–4860
Zhang H, Khurana KK, Zong Q-G, Kivelson MG, Hsu TS, Wan WX, Pu ZY, Angelopoulos V, Cao X, Wang YF, Shi QQ, Liu WL, Tian AM, Tang CL (2012) Outward expansion of the lunar wake: ARTEMIS observations. Geophys Res Lett 39:L18104
Zhang H, Khurana KK, Kivelson MG, Angelopoulos V, Wan WX, Liu LB, Zong Q-G, Pu ZY, Shi QQ, Liu WL (2014) Three-dimensional lunar wake reconstructed from ARTEMIS data. J Geophys Res 119:5220–5243
Zhou X-Z, Angelopoulos V, Poppe AR, Halekas JS (2013) ARTEMIS observations of lunar pickup ions: Mass constraints on ion species. J Geophys Res Planets 118:1766–1774
Zhou X-Z, Angelopoulos V, Poppe AR , Halekas JS, Khurana KK, Kivelson MG, Fatemi S, Holmström M (2014) Lunar dayside current in the terrestrial lobe: ARTEMIS observations. J Geophys Res Space Phys 119:3381–3391
Zimmerman MI, Farrell WM, Stubbs TJ, Halekas JS, Jackson TL (2011) Solar wind access to lunar polar craters: Feedback between surface charging and plasma expansion. Geophys Res Lett 38:L19202
Zimmerman MI, Jackson TL, Farrell WM, Stubbs TJ (2012) Plasma wake simulations and object charging in a shadowed lunar crater during a solar storm. J Geophys Res 117:E00K03
Zimmerman MI, Farrell WM, Stubbs TJ (2013) Recursive plasma wake formation on the Moon and its effect on polar volatiles. Icarus 226:992–998
Zimmerman MI, Farrell WM, Hartzell CM, Wang X, Horányi M, Hurley DM, Hibbits K (2016) Grain-scale supercharging and breakdown on airless regoliths. J Geophys Res Planets 121:2150–2165
Zook, HA, McCoy JE (1991) Large scale lunar horizon glow and a high altitude lunar dust exosphere. Geophys Res Lett 18:2117–2120
Zurbuchen TH, Fisk LA, Gloeckler G, Von Steiger R (2002) The solar wind composition throughout the solar cycle: A continuum of dynamic states. Geophys Res Lett 29:1352

APPENDIX—RECENT DEVELOPMENTS

In the area of atmosphere/exosphere research, there was a recent re-analysis of the LCROSS exospheric plume observations by Mandt et al. (2022). Rather than using molecular compositions, elemental composition ratios were examined, and these ratios were then compared to various possible sources. It was determined that the volatiles in the impact plume originating from the crater floor are likely not volcanic in origin, and better fit an exogenic cometary source.

Also, new dynamic exospheric modeling tools have been developed to predict the global exospheric and surface effects of a lunar lander plume. Prem et al. (2020) found that there are possible global consequences of a landing at high latitudes, with a relatively large fraction of the plume water vapor being capable of migrating into the lunar cold traps, thus creating human contamination. This work was heavily cited by the National Academy's Committee on Planetary Protection (2020) which finds there is a lack of studies to characterize the level of contamination of volatiles that would be harmful to future science investigations of PSR chemical evolution.

In the area of plasma research, there has been recent work on plasma waves in magnetic anomalies. Specifically, electrostatic solitary waves and broadband electric field noises were observed in orbit around a magnetic anomaly on the dayside (Chu et al. 2021; Harada et al. 2021). These waves were attributed to electron two-stream instability and electron cyclotron

drift instability. Solar wind strahl electrons and upward electron beams from the nightside lunar surface are also effective for the generation of broadband electric field noises in the near-lunar wake boundary (Nishino et al. 2022).

Also in plasma research, it was recently suggested that the Moon and Earth were magnetically connected in early times. Recent analysis of Apollo samples suggest the Moon had a substantial global magnetic field structure from ~4.25 to ~2.5 Ga. Given the location of the Moon's magnetosphere within Earth's magnetosphere, modeling by Green et al. (2020) suggests the two bodies were magnetically connected to allow volatiles in the form of an ion plasma to flow along magnetic field lines from the terrestrial ionosphere to the cold trap polar regions of the Moon.

In the area of dust research, there is new work on understanding the surface effect from small, fast Beta-meteoroid impacts. Since the discovery of the Moon's asymmetric ejecta cloud, the origin of its sunward-canted density enhancement has not been well understood. Szalay et al. (2020) suggests that Beta-meteoroids that hit the Moon's sunward side could explain this unresolved asymmetry. Beta-meteoroids are submicron in size, comparable to or smaller than the regolith particles they hit and can impact the Moon at very high speeds ~100 $km \cdot s^{-1}$. This finding suggests Beta-meteoroids may also contribute to the evolution of other airless surfaces in the inner solar system, and by extension, at exozodiacal systems.

REFERENCES

Chu F, Halekas JS, Cao X, McFadden JP, Bonnell JW, Glassmeier K-H (2021) Electrostatic waves and electron heating observed over lunar crustal magnetic anomalies. J Geophys Res 126:e2020JA028880

National Academies of Sciences, Engineering, and Medicine (2020) Report Series: Committee on Planetary Protection: Planetary Protection for the Study of Lunar Volatiles. Washington, DC: The National Academies Press. https://doi.org/10.17226/26029

Green J, Draper D, Boardsen S, Dong C (2020) When the Moon had a magnetosphere. Sci Adv 6:eabc0865

Harada Y, Kasahara Y, Nishino MN, Kurita S, Saito Y, Yokota S, Kumamoto A, Takahashi F, Shimizu H (2021) Global maps of solar wind electron modification by electrostatic waves above the lunar day side: Kaguya observations. Geophys Res Lett 48:e2021GL095260

Mandt KE, Mousis O, Hurley D, Bouquet A, Retherford KD, Magaña LO, Luspay-Kuti A (2022) Exogenic origin for the volatiles sampled by the Lunar Crater Observation and Sensing Satellite impact. Nat Commun 13:642

Nishino MN, Kasahara Y, Harada Y, Saito Y, Tsunakawa H, Kumamoto A, Yokota S, Takahashi F, Matsushima M, Shibuya H, Shimizu H, Miyashita Y, Goto Y, Ono T (2022) An event study on broadband electric field noises and electron distributions in the lunar wake boundary. Earth Planets Space 74:9

Prem, P, Hurley DM, Goldstein DB, Varghese PL (2020) The evolution of a spacecraft-generated lunar exosphere. J Geophys Res 125:e2020JE006464

Szalay JR, Pokorný P, Horányi M (2020) Hyperbolic meteoroids impacting the Moon. Astrophs J Lett 890:L11